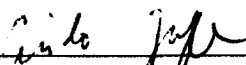


DETECTING METHANE EBULLITION IN WINTER FROM ALASKAN LAKES USING
SYNTHETIC APERTURE RADAR REMOTE SENSING

By

Melanie J. Engram

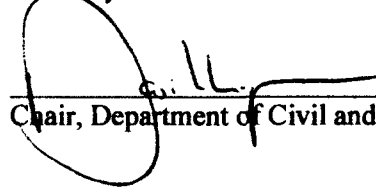
RECOMMENDED:



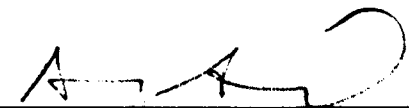


David Verbyla

Katey Walter Anthony
Advisory Committee Chair


Chair, Department of Civil and Environmental Engineering

APPROVED:


Dean, College of Engineering and Mines

Lanene K. Suffy
Dean of the Graduate School

April 11, 2012
Date

**DETECTING METHANE EBULLITION IN WINTER FROM ALASKAN LAKES USING
SYNTHETIC APERTURE RADAR REMOTE SENSING**

A

THESIS

Presented to the Faculty of the University of Alaska Fairbanks

In Partial Fulfillment of the Requirements

for the Degree of

MASTER OF SCIENCE

By

Melanie J. Engram, B.A.

Fairbanks, Alaska

May 2012

Copyright © 2012 Melanie Engram

UMI Number: 3528861

All rights reserved

INFORMATION TO ALL USERS

The quality of this reproduction is dependent upon the quality of the copy submitted.

In the unlikely event that the author did not send a complete manuscript and there are missing pages, these will be noted. Also, if material had to be removed, a note will indicate the deletion.

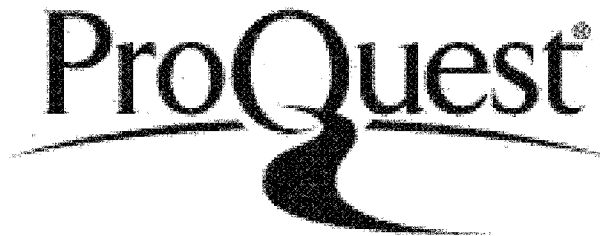


UMI 3528861

Published by ProQuest LLC 2012. Copyright in the Dissertation held by the Author.

Microform Edition © ProQuest LLC.

All rights reserved. This work is protected against unauthorized copying under Title 17, United States Code.



ProQuest LLC
789 East Eisenhower Parkway
P.O. Box 1346
Ann Arbor, MI 48106-1346

Abstract

Methane (CH₄) is a greenhouse gas with a high radiative forcing attribute, yet large uncertainties remain in constraining atmospheric CH₄ sources and sinks. While freshwater lakes are known atmospheric CH₄ sources, flux through ebullition (bubbling) is difficult to quantify *in situ* due to uneven spatial distribution and temporally irregular gas eruptions. This heterogeneous distribution of CH₄ ebullition also creates error when scaling up field measurements for flux estimations. This thesis reviews estimates of CH₄ contribution to the atmosphere by freshwater lakes presented in current literature and identifies knowledge gaps and the logistical difficulties in sampling CH₄ flux via ebullition (bubbling). My research investigates various imaging parameters of space-borne synthetic aperture radar (SAR) to constrain current CH₄ emissions from northern lakes. In a GIS spatial analysis of lakes on the northern Seward Peninsula, Alaska, comparing field data of ebullition to SAR, I found that SAR L-band backscatter from lake ice was high from lakes with CH₄ bubbles trapped by lake ice and low from lakes with low ebullition activity. The 'roughness' component of a Pauli polarimetric decomposition of quad-pol SAR showed a significant correlation with the percentage of lake ice area containing CH₄ bubbles and with CH₄ ebullition flux. This indicates that the mechanism of SAR scattering from ebullition bubbles trapped by lake ice is single bounce. I conclude that SAR remote sensing could improve our ability to quantify lake ebullition at larger spatial scales than field measurements alone, could offer between-lake comparison of CH₄ ebullition activity, and is a potential tool for developing regional estimations of lake-source CH₄.

Table of Contents

	Page
Signature Page	i
Title Page	ii
Abstract	iii
Table of Contents	iv
List of Figures	vii
List of Tables	xi
List of Appendices	xii
Acknowledgements	xiii
Chapter 1 Introduction and research objectives	1
1.1 Methane atmospheric burden	1
1.2 Lakes as CH ₄ emitters	2
1.2.1 Regional and global CH ₄ emission estimates: a review	3
1.2.2 Point source ebullition seeps	6
1.2.3 Knowledge gaps in factors driving methanogenesis	7

1.2.4 Knowledge gaps in factors driving CH ₄ ebullition	8
1.3 Synthetic Aperture Radar (SAR) signal parameters overview	10
1.4 SAR history with lake ice imaging.....	12
1.5 Research objectives	13
1.6 Chapter 1 References.....	16
Chapter 2 Estimating methane ebullition in thermokarst lakes with space-borne synthetic aperture radar (SAR)	22
2.1 Abstract	22
2.2 Introduction	23
2.3 Methods.....	28
2.3.1 Study site.....	28
2.3.2 In-situ field measurements of CH ₄ ebullition bubbles in lake ice.....	28
2.3.3 Comparison of single-pol C-band and L-band SAR for detection of ebullition bubbles in lake ice	30
2.3.4 Using Pauli decomposition of quad-pol L-band SAR to determine the scattering mechanism of ebullition bubbles associated with lake ice	32
2.4 Results	34

2.4.1 Comparison of C-band and L-band SAR.....	34
2.4.2 L-band SAR polarimetric decomposition	35
2.5 Discussion.....	35
2.5.1 C-band and L-band single-polarized SAR and CH ₄	35
2.5.2 Utility of L-band single-polarized SAR as an indicator of ebullition	38
2.5.3 Scattering mechanisms.....	39
2.5.4 Seasonal variability of the Pauli decomposition SAR signal and implications for CH ₄ detection.....	40
2.5.5 Factors that could confound the SAR signal from ebullition bubbles	41
2.6 Conclusions	42
2.7 Acknowledgements	44
2.8 References	45
Chapter 3 General Conclusion	61

List of Figures

	Page
<p>Figure 2.1: a) Example of a CH₄ ebullition bubble cluster trapped in ice on a thermokarst lake, as seen from top of ice and, b) vertical profile of ebullition bubbles, as seen from the side, in a block of clear lake ice. Bubbles frozen in ice commonly have conical shapes with large diameter of the cone facing up. This flattened top is formed as a bubble comes to rest under the lake ice sheet. The pointed tip at the bottom forms as ice freezes around the bubble, squeezing the gas into a point. Clear ice between bubbles indicates a duration of time passing without ebullition. Closely stacked bubbles indicate frequent ebullition events.....</p>	51
<p>Figure 2.2: Study lakes on the thermokarst lake landscape of the northern Seward Peninsula, Alaska, USA. The scarred, mottled appearance in this Landsat TM composite image from the Geographic Information Network of Alaska (GINA) shows a thermokarst lake cycle that has been active since early Holocene. Dark, water filled lakes often overlap lighter, vegetation filled drained lake basins. White stars indicate location of bubble survey transects on early winter lake ice on lake margins with steep shores of yedoma permafrost. Non-starred white lines are locations of transects on shallow lowland margins. Lake names are A) Rhonda Lake, B) Cocker Gap Lake, C) Fox Den Lake, D) Lake Claudi, E) Island Lake, F) Tea Lake, G) Kim Lake, H) Owl Lake, I) Jaeger Lake, and J) Three Loon Lake.</p>	52
<p>Figure 2.3: Methane bubble survey transect on a thermokarst lake as seen a) looking to the west while taking field measurements of size, type and location of bubble clusters through early</p>	

fall lake ice; b) in GIS with DGPS points showing the location of CH₄ seeps with an orthorectified photo reference data (2003) as background. 53

Figure 2.4: Pauli decomposition of fully-polarized SAR allows direct inference as to the scattering mechanism of a target. Classic SAR scattering mechanisms as they could apply to lake ice: single-bounce (roughness), double-bounce and volumetric scattering. Our analysis revealed that the single-bounce component of the Pauli decomposition showed a positive correlation with ebullition bubbles. This schematic, depicting snow (grey stars) on top of lake ice with ebullition bubbles over lake water (grey), with some bubbles ascending in the water column and some resting under the ice, shows the most probable single-bounce interface as indicated by arrows: from ebullition bubbles resting under lake ice. The real components of the dielectric constant (ϵ') for L-band radar frequencies are: $\epsilon' \approx 1$ for gas, $\epsilon' \approx 3.2$ for ice and, $\epsilon' \approx 88$ for cold water in the liquid phase. 54

Figure 2.5: Comparison of single-polarized data from dates close to field measurements in fall 2008. a) C-band SAR ($\sim 23^\circ$ incidence angle, VV polarization, ERS-2) backscatter from lake ice is not correlated with bubble area. Triangles represent values from Oct. 27th, grey squares from Nov. 9th, black diamonds from Nov. 12th, and circles from Nov. 15th. b) L-band SAR (HH, ALOS PALSAR) lake ice backscatter shows significant correlation with the percent of area of lake ice with bubbles. Error bars are +/- one standard deviation. 55

Figure 2.6: Comparison of same day 9-November-2008 SAR images a) L-band (23.6 cm wavelength) and b) C-band (5.6 cm wavelength). Lake ice in the C-band image is much brighter overall and brighter than the land in some cases. Lakes are outlined in white in the C-band image to distinguish lake ice from land. 56

Figure 2.7: Significant positive correlation between single-bounce (roughness) from polarimetric decomposition of L-band quad-polarized data for Nov. 14, 2009 and percent of area of ice showing CH₄ ebullition, as measured in fall 2008. Diamonds show Pauli Band 3 (roughness), ~21° incidence angle; regression equation is Pauli DN = 1.1392*(% bubble area) + 0.3855, R²= 0.771, p = 0.001. Squares show Pauli Band 2 (volumetric scattering) and triangles show Pauli Band 1 (double bounce), neither of which show a correlation with percent of area of lake ice with ebullition bubbles. Error bars are +/- one standard deviation. 57

Figure 2.8: Pauli Band 3 roughness component of L-band PALSAR quad-polarized SAR backscatter from thermokarst lake ice, plotted against long-term (120 day) seasonal CH₄ flux for a) spring and b) fall. Error bars show +/- one standard deviation. Note different scales with higher spring SAR values. 58

Figure A.1: Type 'N' CH₄ bubbles viewed from top with slightly oblique viewing angle (a), and the same bubble group from side profile (b). Notice flat tops of bubble with circular shape, curved bulging sides, tapering to a lens shape or a conical shape at bottom of bubble. Type 'N' bubbles have no vertical layers and are formed when bubbles are released as a single event, not repeated regularly on time scales of days to weeks. The vertical striations in the image are an artifact of cutting ice blocks with a saw. Photos by M. Engram.67

Figure A.2: A vertical column of Type 'A' bubbles as seen from slightly different viewing angles in thick lake ice column. The left photo views the underside of bubbles; the right photo views top and sides of bubbles. Profile measurements from top of ice (cm) are provided on the far right table. Flat circular tops with conical, lenticular, or (rarely), flat bottoms characterize these bubbles which are usually about 1-4 cm in diameter, therefore some of these bubbles are

larger than a typical type 'A'. Blue lines link the same bubbles in both photos and chart. Photos by M. Engram.....	68
Figure A.3: Dimensions, shape and spacing of small Type 'A' methane bubbles, as viewed from side profile. Note conical or lenticular shape. Photo by M. Engram	69
Figure A.4: Type 'B' bubble cluster with merged bubbles and typical circular "bull's eye" pattern. Photo by M. Engram.	69
Figure A.5: Type 'B' methane bubble cluster with non-circular pattern. Photo by M. Engram.	70
Figure A.6: Ice cavity created by strong methane ebullition. This piece of ice was cut from the surface of the lake and inverted for examination. Ridges encircle the main cavity, but are shown most clearly on the left. Ridges measured 1 cm for rise and 1 cm for run and were formed as a result of larger and larger bubbles stacking up underneath the lake ice. Photo by M. Engram.	71

List of Tables

	Page
Table 2.1: Methane ebullition bubble clusters identified in bubbles surveys along transects on early winter lake ice on the northern Seward Peninsula, Alaska, USA.....	59
Table 2.2: SAR data used in single polarity geospatial analysis.....	59
Table 2.3: List of PALSAR fully polarized data (HH, VV, HV and VH) used for analysis with Pauli decomposition. All data were acquired with an incidence angle of 21.5°.	60

List of Appendices

	Page
Appendix A: Report on physical configuration of some types of methane (CH₄) ebullition bubbles in and under lake ice	62
Appendix B: GIS methods for SAR and lake ice analysis.....	72

Acknowledgements

I'm forever grateful for my advisor, Dr. Katey Walter Anthony, who whisked me away from the drudgery of the workforce and into the exciting, unfamiliar world of graduate school. I appreciated Katey's patience, enthusiasm, and ebullience. I depended on her expertise. I learned how to ask hard science questions and follow through to find the answers from Katey.

I'm also grateful for my other committee members. Dr. Franz Meyer, who can speak four languages fluently (English, German, Romulan and Polite German), taught me about SAR and about the excitement of scientific investigation. Dr. Guido Grosse encouraged me to have confidence in my work and precision in my thought and organization. Dr. Dave Verbyla, a longtime geospatial hero of mine, posed thought-provoking questions that sent me working into all hours of the night.

I'm so grateful for my loving family. Thanks to my life partner and soul mate, Arch Gayle, who encouraged me while I earned this degree and who uncomplainingly picked up the slack while I was in the field or out of town for conferences, and to our sweet daughter Madeline for going with the flow.

I thank Lawrence Plug, Chris Arp, Laura Oxtoby, Louise Farquharson, Ben Jones, and Amy Strohm for assistance with field data collection; Lawrence Plug for collecting and processing differential global positioning system (DGPS) field data; and Ronnie Daanen for coordination with Ice Alaska. I thank CH2M Hill Polar Services (CPS) for field logistics during our 2008 fall field campaign.

I thank the knowledgeable staff at the Alaska Satellite Facility (ASF), Michelle Harbin, Bill Hauer, Jessica Garron, and the rest of ASF's User Services Office staff for assistance with data

ordering and satellite tasking. Thanks to ASF's User Tool Development group, particularly Rudi Gens and Kirk Hogenson with their fast action in resolving software issues. Thanks to Wade Albright for expert consultation in obscure SAR documentation of peak-to-side-lobe ratios. I thank both sides of the ASF 'house', the National Aeronautics and Space Administration's Distributed Data Archive Center and JAXA's (Japan Aerospace exploration Agency's) Americas ALOS Data Node for access to SAR data. I acknowledge the German Aerospace Center (DLR) for providing TerraSAR-X data through their generous International Polar Year grant.

I thank Anthony Dulgeris for polarimetric assistance. Thanks to Dave Podrasky, Jason Geck and Barbara Truessel from my peer writing group and Kim Morris for invaluable assistance with manuscript review and editing.

Access to field sites on the Bering Land Bridge National Preserve was granted by the National Parks Service (permit # BELA-2008-SCI-0002). Funding was provided by NASA Carbon Cycle Sciences NNX08AJ37G and NNX11AH20G and NSF IPY #0732735.

Chapter 1 Introduction and research objectives

1.1 Methane atmospheric burden

Understanding the sources and sinks of methane (CH₄), a potent greenhouse gas, has become increasingly important in a warming world. Since CH₄ in the atmosphere has 25-28 times the global warming potential of carbon dioxide (CO₂) on a 100 year time horizon (Boucher et al. 2009), it is important to identify and quantify sources of atmospheric CH₄ more accurately than current approximations. Although the concentration of CH₄ in the atmosphere for the last 800 thousand years, as recorded in polar ice cores, has ranged from 350 to 700 parts per billion by volume (ppbv) (Chappellaz et al. 1993; Li et al. 2010; Louergue et al. 2008; Petit et al. 1999), the current atmospheric concentration of CH₄ is over twice these prehistoric levels, with a global average of 1,799 ppbv of CH₄ in 2010 (NOAA News, 2011). Historically, the atmospheric CH₄ level has risen in the last three decades, as seen by direct measurement through a global CH₄ observation network. Methane increased from ~1610 ppbv in 1983 to ~1750 ppbv in 1999, followed a period of non-growth from 1999-2006 (Dlugokencky et al. 1994, 2009). Methane levels began increasing again in 2007 (Dlugokencky et al. 2011), but at a slower rate. The variable rates of CH₄ increase and the nine-year steady state of atmospheric CH₄ underscore current uncertainties and knowledge gaps in CH₄ sources and sinks. Recent work based on ¹³C/¹²C isotopic ratios of atmospheric CH₄ indicates that the early 2000's plateau of CH₄ concentration in the atmosphere is not consistent with a slowdown in combustion of fossil fuels, but rather indicates reduced biogenic sources in the northern hemisphere (Kai et al. 2011).

1.2 Lakes as CH₄ emitters

Estimated global emission of CH₄ to the atmosphere, based on NOAA *in situ* measurements, is approximately 556 ± 10 Tg CH₄ yr⁻¹ (Dlugokencky et al. 2011, Dlugokencky n.d.). Some major sources of CH₄ to the atmosphere have been identified as wetlands, termites, domesticated animals, rice agriculture, natural gas, and biomass burning (Chen and Prinn 2006). Lake-source CH₄ has yet to be included in the global CH₄ budget (IPCC 2007). While bottom-up estimates based on field studies suggest that lakes are a significant source of biogenic CH₄ to the atmosphere (Bastviken et al. 2004; Semiletov 1999; Walter et al. 2006; Zimov et al. 1997), the difficulty of directly measuring lake CH₄ emissions has allowed only rough, first-order quantification. In contrast to northern wetlands, which often stop producing CH₄ in the winter when they freeze, many lakes have unfrozen sediments and can produce CH₄ all year long. Large quantities of lake-sourced CH₄ can be released to the atmosphere at spring melt (Phelps et al. 1998; Strayer and Tiedje 1978; Walter Anthony et al. 2010). Lakes are a conspicuous landscape feature, covering > 3% of global land area (Downing et al. 2006). This recent GIS assessment of global land/water cover by Downing et al. (2006) indicates a previous underestimation of surface area of small lakes, which are particularly prolific CH₄ producers.

Methane is formed by microbes in lake bottom sediments through anaerobic decomposition of organic matter (Mah et al. 1982) and is released from lakes to the atmosphere through several transport mechanisms: ebullition, lake turnover, diffusion and plant transport (Bastviken et al. 2011). Some first order quantifications of northern lake CH₄ emissions to the atmosphere include those of Walter et al. (2007) whose scaled-up field measurements indicate that lakes north of 45° N latitude contribute 24 ± 10 Tg C yr⁻¹ to the atmospheric burden, and

from Bastviken et al. (2011) who estimated lakes north of 54° N latitude emit 13 ± 12 Tg C yr⁻¹. According to the authors this latter estimate is conservative due to the underestimation of ebullition and plant flux. The former estimate is likely an overestimate due to inaccuracies in the delineation of different lake types and generations and in pan arctic lake area. A current global estimate of lake-sourced CH₄, omitting rivers and reservoirs, is 72 ± 44 Tg C yr⁻¹ which is up to 21% of all global sources (Bastviken et al. 2011).

1.2.1 Regional and global CH₄ emission estimates: a review

Bastviken et al. (2011) incorporated data from other studies with their own field measurements and generated estimates for regional CH₄ fluxes by multiplying an average CH₄ flux by the area of lakes in the latitudinal regions provided by Downing and Duarte (2009). Data were included from studies on the grounds that they distinguished between four modes of emission (ebullition, diffusion, plant transport and CH₄ stored in the stratified lake water released at seasonal lake turnover), but the chosen studies weren't required to include measurements of all emission modes. Some of the included studies measured only diffusion; some studies measured combined ebullition and diffusion with fixed or roving chambers placed in different zones of lakes, but not specifically over ebullition seeps; and some studies measured point-source ebullition with fixed bubble traps placed over discrete ebullition seeps.

Bastviken et al. (2011) provide a latitudinal breakdown of CH₄ emissions as follows: the highest lake-source CH₄ emitting latitudinal range is 25°-54° (temperate) at 31.6 Tg yr⁻¹, second highest is 0°-24° (tropical) at 26.6 Tg yr⁻¹ with the 54°-66° (sub-polar) and >66° (arctic, since no southern hemisphere lakes south of 54° were included) latitudes estimated at 6.6 and 6.8 Tg yr⁻¹ respectively. These estimates suggest that CH₄ flux from tropical and temperate lakes are about 4

times higher than sub-polar and arctic lakes. This difference is even more pronounced when the area of lakes is considered: the sub-polar zone (54° - 66°) with the smallest CH_4 flux estimation from lakes has the greatest lake area (Lehner and Döll 2004, Downing and Duarte 2009). The question arises to what degree tropical lakes really are more prolific CH_4 emitters than lakes in the sub-polar/arctic zones and to what degree is this difference in CH_4 estimations due to incomplete data sets and differences in types of flux measurements (ebullition, diffusion, plant transport, stratification storage) for each lake?

Differences in these latitudinal estimates in Bastviken et al. (2011) might be related to the mode of CH_4 emission that was measured. For many lakes, as reported in the supplementary online material (SOM), no ebullition flux measurements were conducted. Yet ebullition is recognized as the dominant pathway for CH_4 emissions from lakes, contributing up to 90% (Bastviken et al. 2010) to 96% (Casper et al. 2000; Walter et al. 2006) of total CH_4 flux at some study sites. Therefore, omitting ebullition flux measurements will skew the total flux estimates toward a too low value. In the sub-polar and northern zone ($> 54^{\circ}$ N), which had the lowest total CH_4 estimates, only 8% of the lakes sampled included ebullition measurements, while 49% of the lakes from the temperate and tropical zones ($< 54^{\circ}$) included ebullition measurements (Bastviken et al. 2011, SOM).

Same tropical lake systems in the Amazon River area, all with high ebullition flux samples, were included several times for this synthesis analysis: the Lago Calado lake system had 65% of total flux attributed to ebullition in one study (Engle and Melack 2000), and 85% CH_4 flux attributed to ebullition in another study (Devol et al. 1988), and a nearby lake system attributed 49% of total flux to ebullition (Bartlett et al. 1990). The Pantanal, one of the world's

largest wetlands that lies largely in Brazil, was cited twice. While these lake systems cover vast areas and multiple inclusions could be valid, duplication of tropical lakes could also indicate a lack of geographically diverse lake sampling data in the tropical region. Bastviken et al. (2011) point out a small sample size for large measured values as a limitation to the flux estimates and as a need for more data collection.

Sparse geographic distribution of CH₄ study lakes is not limited to the tropics. Since data to be included in the synthesis by Bastviken et al. (2011) were chosen for their discrimination between CH₄ transport types, the study lakes are not spatially well-distributed nor geographically representative of different types of lakes from different northern regions. Lakes sampled from North America include lakes from Alaska, Canada, New York State, and Wisconsin only. European lakes are limited to Swedish and Finish lakes. The only Asian lakes included are in Siberia. More geospatially diverse data are needed, along with lake measurements from various types of lakes.

There is considerable lack of measurement of ebullition flux in many studies. This lack of data is the result of the difficulty of measuring temporally sporadic and unevenly spaced bubbling events of a colorless, odorless gas from the lake surface that is often ruffled by breeze or winds. The majority of those studies that did measure ebullition flux used roving chambers deployed over short periods of time, intended for diffusive flux measurements. While diffusive flux and ebullitive flux can be separated in non-stationary floating chamber measurements, either statistically or using physical means to separate diffusion and ebullition contributions (Bastviken et al. 2010), a roving gas collection chamber has a high probability to miss point source ebullition CH₄ seeps (Walter et al. 2006) or else move over them too quickly to measure all the CH₄ that a

fixed seep emits in a single ebullition event. Stationary traps anchored directly over CH₄ seeps provide a more accurate measurement of actual flux from ebullition in northern lakes, where CH₄ seeps are observed to occur in a discrete geographic location in lakes (Walter et al. 2006, Walter Anthony et al. 2010). In Bastviken et al. (2011, SOM), the three highest ebullition flux rates, regardless of latitude, all used stationary underwater inverted funnels to trap and measure the gas: Casper et al. (2000) reported 4,526 mmol CH₄ m⁻² yr⁻¹ from ebullition on Priest Pot Lake in Europe. Strayer and Tiedje (1978) reported 3,042 mmol CH₄ m⁻² yr⁻¹ from ebullition on Wintergreen Lake in Michigan, USA. Walter Anthony et al. (2010) report an average of 72,938 mmol CH₄ seep⁻¹ yr⁻¹ measured with static underwater gas traps from the strongest type of ebullition seep that is less than 1m² in northern lakes. Bastviken et al. (2010) calls for future measurements using static floating chambers to determine within lake variability in order to take CH₄ samples that are representative of the whole lake or lake system.

1.2.2 Point source ebullition seeps

The phenomenon of relatively stationary point source CH₄ ebullition seeps, as observed in northern thermokarst lakes, has been explained as a result of gas pushing through consolidated substrate and creating tunnels and bubble tubes through sediments (Mattson and Likens 1990; Scandella et al. 2011). Gas continues to travel along these established pathways of lesser resistance, resulting in ebullition bubbles erupting repeatedly from the same point on the lake bed. The size of substrate granules and resulting consolidation has also been studied in the laboratory to help determine the affect of substrate type on CH₄ storage and release (Meier et al. 2011). Using $\delta^{13}\text{C}_{\text{CH}_4}$, $\delta\text{D}_{\text{CH}_4}$, and radiocarbon dates of CH₄, Walter et al. (2008a) demonstrated that low-flux seeps in northern thermokarst lakes originate from surface sediments, which tend to be more

loosely packed, while stronger ebullition seeps originate from deeper, more densely packed loess-dominated sediments. Further research is needed to provide more insight into the transport of CH_4 from deep lake substrate, upward to the point source seep in the lake bottom to help explain how, why and when these seeps shut down or move and how ebullition is expressed in lakes with varying sediment types and densities. Walter Anthony et al. (2010) reported point-source ebullition seeps in northern thermokarst lakes to stay in the same place for at least 8 years. Some questions to consider with future lake-source CH_4 ebullition research emerge: are stationary seeps a northern lake phenomenon or a phenomenon of lakes with dense, silty substrate, such as loess? Could groundwater dynamics alter CH_4 seepage pathways? It is currently uncertain if tropical and temperate lakes have more loosely consolidated substrate that could also lend itself to more frequent changes in CH_4 tubular pathways in sediments, potentially giving rise to more accurate measurements from floating as opposed to fixed collection chambers.

1.2.3 Knowledge gaps in factors driving methanogenesis

Substrate availability and temperature are two important factors that influence the rate of methanogenesis. In wetlands, temperature and available organic carbon together can explain 100% of CH_4 flux variations (Christensen et al. 2003). If the latitudinal difference in CH_4 flux from lakes is real, and not just an artifact of measurement methods, an explanation for this difference would most likely also include temperature and organic carbon availability as driving forces. Organic matter availability is a limiting factor in CH_4 production, since methanogenesis requires fuel. Labile organic carbon as fodder for methanogenic microbes, archaea, is correlated to CH_4 production in lakes (Bastviken et al. 2010) and wetlands (Whiting and Chanton 1993). Among northern thermokarst lakes, organic-rich permafrost is also an important source of labile

organic matter fueling methanogenesis (Zimov et al. 2006). It is probable that warmer, eutrophic lakes in temperate and tropical zones could emit more CH_4 than lakes from high latitudes on an area-normalized basis due to higher availability of organic substrates and warm temperatures. In one incubation study, CH_4 emissions increased 100-fold with a 26°C increase in temperature, from 4°C to 30°C (Duc et al. 2010). But taken by itself, temperature has been found to be inadequate to explain methanogenesis variations in rice paddies (Schutz et al. 1990). Perhaps autochthonous organic matter plays a more important role in fueling methanogenesis in tropical and temperate lakes than in sub-polar and arctic lakes, the latter of which are less productive. Conversely, temperature increases could cause enhanced availability of organic matter from thawing permafrost, increasing CH_4 production in northern lakes. Major knowledge gaps exist about the role of temperature and available organic carbon in methanogenesis in lakes, and if these variables play different roles in arctic versus tropical lakes.

1.2.4 Knowledge gaps in factors driving CH_4 ebullition

Ebullition is difficult to measure, even when measuring flux directly over a seep in the water column, due to the sensitivity of ebullition to changes in surface air pressure. Lake-bed substrate acts as a short-term storage container for free-state CH_4 gas and water containing dissolved CH_4 . A drop in hydrostatic pressure increases ebullition activity both by changing the volume that the free phase gas occupies in sediments, and by changing the solubility of dissolved CH_4 . This drop in hydrostatic pressure could be a result of a drop in water level (Bartlett et al. 1988) and/or a drop in surface air pressure (Casper et al. 2000; Mattson and Likens 1990). Short-term measurements using bubble-traps placed directly over point source seeps during low atmospheric pressure could show an elevated flux while measurements taken during a high

atmospheric pressure episode will likely cause an under-representation of the long-term average daily flux (Vas 2010). This response to air pressure is a hysteretic effect, since a low pressure event following a long period of high pressure will likely yield more bubbles due to bubble storage in the lake-bed sediments than would a subsequent low pressure event occurring after the lake-bed has been depleted of free-phase gas (Varadharajan 2009). More research is needed to learn enough about the air-pressure/ebullition-volume relationship in order to correct for the air-pressure effect on the ebullition gas volumes measurements at any given moment of time. To circumvent the confounding factor of air pressure, in my work (Chapter 2) I averaged flux measurements over time windows ≥ 120 days, with the idea that measurements averaged over this long a time period will naturally be normalized and not dependent on individual air pressure events.

Ebullition is hard to locate during open water conditions where wind and waves can obscure bubbles erupting on the water surface. Methane ebullition estimation is facilitated by taking advantage of lake ice freezing around bubbles in early winter in northern lakes, arresting motion and displaying a visual record of the gas emergence rate (Walter et al. 2006). Ice that is directly above slower emitting gas seeps will exhibit small bubbles that are vertically separated by layers of ice. Ice above more prolific gas seeps will show larger bubbles, a result of smaller bubbles accumulating under the existing ice sheet so fast that they merge before ice can form around them. Over the highest flux seeps, ice formation is often precluded by a combination of vigorous bubbling action and convection of warmer water from the lake bottom to the surface by the bubbles. This maintains a hole in the ice where open, bubbling water can be seen all winter, or covered with only a thin lens of ice. Bubble surveys in which each frozen bubble cluster is

categorized and its area measured along transects on early winter lake ice provide valuable data from which to extrapolate whole-lake and first-order regional CH₄ ebullition estimates (Walter Anthony et al. 2010).

Measuring ebullition is logistically challenging, even when using the freezing process to quantify CH₄ ebullition with bubble surveys. Access to remote lakes is expensive and time intensive, often involving travel across boggy ground in the summer, or sub-freezing temperatures in the winter. While frozen bubbles can be seen trapped in lake ice, snow cover or white ice often obscure patches of bubbles. Linear transects across ice can miss spatially patchy bubble clusters, while clearing a wider area from snow to survey a larger area to insure thorough sampling is so labor and time intensive as to be prohibitive on all lakes. Vertical aerial photography taken immediately after freeze-up can help determine presentations of bubbles in the surface of ice, but may not be able to differentiate well between a lone single-layer bubble that represents negligible flux and vertically layered bubbles that are a result of gas release over time (flux). Aerial vertical photography is also limited to what is typically a narrow window of time with snow-free conditions following freeze up. Microwave remote sensing, specifically the active instrument of synthetic aperture radar (SAR) shows a correlation with CH₄ ebullition bubbles trapped by lake ice (Walter et al. 2008b and this work).

1.3 Synthetic Aperture Radar (SAR) signal parameters overview

Synthetic Aperture Radar (SAR) is an active sensor, supplying its own source of illuminating energy in the form of microwave pulses. SAR is therefore a valuable remote sensing tool for the Arctic since it does not require illumination from the sun and can image 24 hours a

day during summer and dark winter. SAR is also independent from the cloud-free skies optical imagery depends on.

SAR instruments have a variety of imaging parameters that include wavelength, polarization, incidence angle, view direction, spatial resolution and temporal resolution (data availability). Each of these variables can change the effectiveness of SAR to supply information about a target. Shorter wavelengths of SAR have less penetrating power, while longer wavelengths penetrate vegetative canopies to reflect from the ground (Ulaby et al. 1986). Each scientific application, for instance soil moisture estimation (Bourgeau-Chavez et al. 2007; Nolan et al. 2003), ocean processes (Li et al. 2005), and sea ice monitoring (Kwok et al. 1990; Martin et al. 2004) has established SAR parameters that best returns information about the scientific target. Radar pulses from a SAR sensor interact with targets on Earth and reflect the microwaves back to the receiver (in a monostatic system) depending on the shape, size and the dielectric constant of the target. The radar signal is either reflected away from the satellite, back to the receiver (backscatter), or the polarization can be changed upon target interaction. Knowledge of target properties such as target size in relation to the sensor's wavelength, the dielectric constant of the target, and the roughness of the target, assist to anticipate the type of backscatter signal or normalized radar cross-section from a target. Once a set of imaging parameters has been established as optimal for providing information on a specific target, this combination of wavelength, polarization and incidence angle can be used to monitor processes or to detect change.

One of the biggest limiting factors in the use of SAR is data availability. Since the SAR instrument is active, energy requirements prohibit continuous imaging, as is possible with optical

remote sensing. SAR imaging must be scheduled for the satellite leaving temporal and spatial holes in global coverage. Since SAR satellites are typically polar orbiting, more SAR data is collected in the Polar Regions due to increased overlap of neighboring acquisitions at high latitudes than at temperate and equatorial locations.

1.4 SAR history with lake ice imaging

SAR and real aperture radars have been used to study lake ice. Starting in the late 1970's, Side Looking Airborne Radar (SLAR) was used to image frozen thermokarst lakes on the Arctic Coastal Plain in Alaska. A dramatic difference in SLAR brightness was noticed in images between lakes that froze to the bottom of the lake bed and those that did not: lakes with floating ice had much higher backscatter than lakes with grounded ice (Mellor 1982; Sellmann et al. 1975; Weeks et al. 1978, 1977). The advent of space-borne SAR also showed higher backscatter from floating ice and lower backscatter from grounded lake ice. This phenomenon was observed with C-band (5.6 cm wavelength) single-polarized VV (vertical transmit/vertical receive) SAR from the European satellites ERS-1 and ERS-2 (Jeffries et al. 1994; Morris et al. 1995) and with C-band HH (horizontal transmit/horizontal receive) SAR from the Canadian satellite Radarsat-1 (Duguay et al. 2002). The most widely accepted theory to explain the large difference in backscatter values from floating and grounded lake ice is that small (millimeter scale) vertically oriented bubbles play a large role in SAR backscatter. These small tubular bubbles in the ice, formed by the rejection of dissolved gasses during the freezing process, is thought to re-direct the strong specular reflection from the ice-water interface back to the SAR receiver.

1.5 Research objectives

The aim of this work is to establish which SAR imaging parameters, if any, are most useful to quantify CH₄ ebullition bubbles trapped by lake ice. By using SAR to constrain current CH₄ emissions via ebullition, we can look at within-lake and between-lake variability in northern climate regions where lakes freeze over. The detection and quantification of CH₄ ebullition in remote sensing images could allow for better spatial coverage within lakes, as compared to the spatially limited ground survey transects, to provide insights on within-lake differences that maybe associated with bathymetry, aspect, currents, erosion, thermokarst activity, talik morphology, age of lake portions, and allochthonous or autochthonous organic matter deposition. SAR analysis could be useful for detecting variances between lakes within a single region, and perhaps lead to a greater understanding of processes that cause differences in CH₄ ebullition among lakes, such as variances in organic carbon availability among different thermokarst lakes types.

This study was intended to explore the feasibility of using SAR as a tool to estimate CH₄ emissions from northern lakes that freeze in the winter. The spatial scale of space-borne SAR, with swath width on the order of 100 km, lends itself to regional-scale observations of freshwater lakes, a scale that could theoretically assist in scaling up *in situ* measurements of CH₄ emissions from lakes to regional estimates of the amount of CH₄ contributed to the atmosphere through ebullition.

In a previous pilot study, we demonstrated the sensitivity of C-band (5.6 cm wavelength) SAR to CH₄ flux and to the area of ebullition bubble clusters trapped by lake ice, as measured along transects surveyed in field campaigns on lakes near Toolik Field Station, Alaska (Walter et

al. 2008b). Radarsat-1 Standard 3 beam mode with an incidence angle of $\sim 34^\circ$, C-band and single polarized HH was the combination of SAR parameters that showed a significant correlation with CH_4 ebullition bubble area ($R^2 = 0.68$) and with CH_4 flux from ebullition ($R^2 = 0.59$) on study lakes near Toolik, Alaska. Although preliminary results are promising, it is unknown if SAR is scattering from CH_4 ebullition bubbles or from other possible confounding targets on or within the lake ice, such as cracks, ice ridges or aquatic plant frozen in the ice.

At the time of this project, a variety of SAR data with different imaging parameters was available for scientific use, yet data availability for specific dates using specific imaging parameters was limited. We tasked new acquisitions with space-borne SAR with three different wavelengths over study sites: the smallest, highest frequency X-band (3.1 cm \approx 9.6 GHz) from the German Space Agency (DLR) satellite TerraSAR-X, C-band (5.6 cm \approx 5.3 GHz) from the European Space Agency (ESA) European Remote Sensing Satellite-2 (ERS-2), and the longest wavelength with the lowest frequency L-band (23.6 cm \approx 1.3 GHz) from the Japanese Space Agency (JAXA) Advanced Land Observing Satellite (ALOS). In addition to new acquisitions from these platforms, we had access to archive data over study sites of C-band SAR from the Canadian Space Agency (CSA) satellite RADARSAT-1. While these data were acquired with a variety of incidence angles and polarizations, data availability was limited by repeat orbit frequencies which are 11, 24, 35 and 46 days repeat cycle, depending on the satellite (listed in order: TerraSAR-X, RADARSAT-1, ERS-2 and ALOS). Data availability was also limited by lack of final scheduling control for all of these SAR satellites, since a satellite acquisition plan with prioritized areas of imaging and prioritized imaging beam modes is decided upon by the

flight agencies that own and control the spacecraft, none of which is the US space agency, NASA.

Since ebullition is such a prolific method of gas transport in lakes, attaining more accurate ebullition estimations would greatly improve regional and global estimations of CH₄ efflux from lakes. One of the main obstacles to providing accurate lake-source CH₄ estimates is the lack of CH₄ ebullition measurements from lakes, due to the logistical challenge and lack of standardized methodology for CH₄ ebullition measurement. If we determined that optical, thermal or microwave remote sensing could help quantify CH₄ emissions from lakes, then either aerial or space-borne remote sensing could be a valuable tool in scaling up local ebullition flux measurements to regional scale CH₄ emission estimates.

1.6 Chapter 1 References

- Bartlett, K.B., Crill, P., Bonassi, J.A., Richey, J.E., & Harris, R. (1990). Methane flux From the Amazon River Floodplain: Emissions during rising water. *Journal of Geophysical Research*, *95*, 773-788
- Bartlett, K.B., Crill, P.M., Sebacher, D.I., Harriss, R.C., Wilson, J.O., & Melack, J.M. (1988). Methane flux from the central Amazonian floodplain. *Journal of Geophysical Research-Atmospheres*, *93*, 1571-1582
- Bastviken, D., Cole, J., Pace, M., & Tranvik, L. (2004). Methane emissions from lakes: Dependence of lake characteristics, two regional assessments, and a global estimate. *Global Biogeochemical Cycles*, *18*, GB4009
- Bastviken, D., Santoro, A.L., Marotta, H., Pinho, L.Q., Calheiros, D.F., Crill, P., & Enrich-Prast, A. (2010). Methane Emissions from Pantanal, South America, during the Low Water Season: Toward More Comprehensive Sampling. *Environmental Science & Technology*, *44*, 5450-5455
- Bastviken, D., Tranvik, L.J., Downing, J.A., Crill, P.M., & Enrich-Prast, A. (2011). Freshwater Methane Emissions Offset the Continental Carbon Sink. *Science*, *331*, 50-50
- Boucher, O., Friedlingstein, P., Collins, B., & Shine, K.P. (2009). The indirect global warming potential and global temperature change potential due to methane oxidation. *Environmental Research Letters*, *4*, 1-6
- Bourgeau-Chavez, L.L., Alden, S., Cella, B., Kwart, M., Murphy, K., & Riordan, K. (2007). Improving the prediction of wildfire potential in boreal Alaska with satellite imaging radar. *Polar Record*, *43*, 321-330
- Casper, P., Maberly, S.C., Hall, G.H., & Finlay, B.J. (2000). Fluxes of methane and carbon dioxide from a small productive lake to the atmosphere. *Biogeochemistry*, *49*, 1-19
- Chappellaz, J., Blunier, T., Raynaud, D., Barnola, J.M., Schwander, J., & Stauffer, B. (1993). Synchronous changes in atmospheric CH₄ and Greenland climate between 40-KYR and 8-KYR BP. *Nature*, *366*, 443-445
- Chen, Y.H., & Prinn, R.G. (2006). Estimation of atmospheric methane emissions between 1996 and 2001 using a three-dimensional global chemical transport model. *Journal of Geophysical Research-Atmospheres*, *111*, D10307

- Christensen, T.R., Ekberg, A., Strom, L., Mastepanov, M., Panikov, N., Oquist, M., Svensson, B.H., Nykanen, H., Martikainen, P.J., & Oskarsson, H. (2003). Factors controlling large scale variations in methane emissions from wetlands. *Geophysical Research Letters*, *30*, 1414
- Devol, A.H., Richey, J.E., Clark, W.A., King, S.L., & Martinelli, L.A. (1988). Methane emission to the troposphere from the Amazon floodplain. *Journal Geophysical Research*, *93*, 1583-1592
- Dlugokencky, E.J. (n.d.). Methane (CH₄). National Oceanic and Atmospheric Administration Earth System Research Laboratory. Retrieved March 29, 2012 from <<http://www.esrl.noaa.gov/research/themes/forcing/Methane.pdf>>.
- Dlugokencky, E.J., Bruhwiler, L., White, J.W.C., Emmons, L.K., Novelli, P.C., Montzka, S.A., Masarie, K.A., Lang, P.M., Crotwell, A.M., Miller, J.B., & Gatti, L.V. (2009). Observational constraints on recent increases in the atmospheric CH₄ burden. *Geophysical Research Letters*, *36*, L18803
- Dlugokencky, E.J., Nisbet, E.G., Fisher, R., & Lowry, D. (2011). Global atmospheric methane: budget, changes and dangers. *Philosophical Transactions of the Royal Society a-Mathematical Physical and Engineering Sciences*, *369*, 2058-2072
- Dlugokencky, E.J., Steele, L.P., Lang, P.M., & Masarie, K.A. (1994). The growth-rate and distribution of atmospheric methane. *Journal of Geophysical Research-Atmospheres*, *99*, 17021-17043
- Downing, J.A., & Duarte, C.M. (2009). *Encyclopedia of Inland Waters*. Oxford: Elsevier
- Downing, J.A., Prairie, Y.T., Cole, J.J., Duarte, C.M., Tranvik, L.J., Striegl, R.G., McDowell, W.H., Kortelainen, P., Caraco, N.F., Melack, J.M., & Middelburg, J.J. (2006). The global abundance and size distribution of lakes, ponds, and impoundments. *Limnology and Oceanography*, *51*, 2388-2397
- Duc, N.T., Crill, P., & Bastviken, D. (2010). Implications of temperature and sediment characteristics on methane formation and oxidation in lake sediments. *Biogeochemistry*, *100*, 185-196
- Duguay, C.R., Pultz, T.J., Lafleur, P.M., & Dray, D. (2002). RADARSAT backscatter characteristics of ice growing on shallow sub-Arctic lakes, Churchill, Manitoba, Canada. *Hydrological Processes*, *16*, 1631-1644

- Engle, D., & Melack, J.M. (2000). Methane emissions from an Amazon floodplain lake: Enhanced release during episodic mixing and during falling water. *Biogeochemistry*, 51, 71-90
- Intergovernmental Panel on Climate Change (IPCC) (2007), *Climate Change 2007: The Physical Science Basis: Contribution of Working Group I to the Fourth Assessment Report of the Intergovernmental Panel on Climate Change*, edited by S. Solomon et al., Cambridge Univ. Press, New York.
- Jeffries, M.O., Morris, K., Weeks, W.F., & Wakabayashi, H. (1994). Structural and stratigraphic features and ERS 1 synthetic aperture radar backscatter characteristics of ice growing on shallow lakes in NW Alaska, winter 1991-1992. *Journal of Geophysical Research-Oceans*, 99, 22459-22471
- Kai, F.M., Tyler, S.C., Randerson, J.T., & Blake, D.R. (2011). Reduced methane growth rate explained by decreased Northern Hemisphere microbial sources. *Nature*, 476, 194-197
- Kwok, R., Curlander, J.C., McConnell, R., & Pang, S.S. (1990). An ice-motion tracking system at the Alaska SAR Facility. *IEEE Journal of Oceanic Engineering*, 15, 44-54
- Lehner, B., & Döll, P. (2004). Development and validation of a global database of lakes, reservoirs and wetlands. *Journal of Hydrology*, 296, 1-22
- Li, J.L., Xu, B.Q., Yao, T.D., Wang, N.L., & MacClune, K. (2010). Atmospheric Methane over the Past 2000 Years from a Sub-tropical Ice Core, Central Himalayas. *Journal of Mountain Science*, 7, 1-14
- Li, X.F., Li, C.Y., Pichel, W.G., Clernente-Colon, P., & Friedman, K.S. (2005). Synthetic aperture radar imaging of axial convergence fronts in Cook Inlet, Alaska. *IEEE Journal of Oceanic Engineering*, 30, 543-551
- Louergue, L., Schilt, A., Spahni, R., Masson-Delmotte, V., Blunier, T., Lemieux, B., Barnola, J.M., Raynaud, D., Stocker, T.F., & Chappellaz, J. (2008). Orbital and millennial-scale features of atmospheric CH₄ over the past 800,000 years. *Nature*, 453, 383-386
- Mah, R.A., Kuenen, J.G., & Quayle, J.R. (1982). Methanogenesis and methanogenic partnerships. *Philosophical Transactions of the Royal Society of London Series B-Biological Sciences*, 297, 599-616

- Martin, S., Drucker, R., Kwok, R., & Holt, B. (2004). Estimation of the thin ice thickness and heat flux for the Chukchi Sea Alaskan coast polynya from Special Sensor Microwave/Imager data, 1990-2001. *Journal of Geophysical Research-Oceans*, 109, C10012
- Mattson, M.D., & Likens, G.E. (1990). Air-Pressure and methane fluxes. *Nature*, 347, 718-719
- Meier, J.A., Jewell, J.S., Brennen, C.E., & Imberger, J. (2011). Bubbles emerging from a submerged granular bed. *Journal of Fluid Mechanics*, 666, 189-203
- Mellor, J. (1982). Bathymetry of Alaskan Arctic Lakes: A key to resource inventory with remote sensing methods. *Ph.D. Thesis, Institute of Marine Science, University of Alaska*, 342 pp
- Morris, K., Jeffries, M.O., & Weeks, W.R. (1995). Ice processes and growth history on Arctic and sub-arctic lakes using ERS-1 SAR data. *Polar Record*, 31, 115-128
- National Oceanic and Atmospheric Administration News. (2011). NOAA greenhouse gas index continues climbing. Retrieved March 29, 2012, from <http://www.noaanews.noaa.gov/stories2011/20111109_greenhousegasindex.html>.
- Nolan, M., Fatland, D.R., & Hinzman, L. (2003). DInSAR measurement of soil moisture. *IEEE Transactions on Geoscience and Remote Sensing*, 41, 2802-2813
- Petit, J.R., Jouzel, J., Raynaud, D., Barkov, N.I., Barnola, J.M., Basile, I., Bender, M., Chappellaz, J., Davis, M., Delaygue, G., Delmotte, M., Kotlyakov, V.M., Legrand, M., Lipenkov, V.Y., Lorius, C., Pepin, L., Ritz, C., Saltzman, E., & Stievenard, M. (1999). Climate and atmospheric history of the past 420,000 years from the Vostok ice core, Antarctica. *Nature*, 399, 429-436
- Phelps, A.R., Peterson, K.M., & Jeffries, M.O. (1998). Methane efflux from high-latitude lakes during spring ice melt. *Journal of Geophysical Research-Atmospheres*, 103, 29029-29036
- Scandella, B.P., Varadharajan, C., Hemond, H.F., Ruppel, C., & Juanes, R. (2011). A conduit dilation model of methane venting from lake sediments. *Geophysical Research Letters*, 38, L06408
- Schutz, H., Seiler, W., & Conrad, R. (1990). Influence of soil-temperature on methane emission from rice paddy fields. *Biogeochemistry*, 11, 77-95
- Sellmann, P.V., Weeks, W.F., & Campbell, W.J. (1975). Use of Side-Looking Airborne Radar to Determine Lake Depth on the Alaskan North Slope. Special Report No. 230. Hanover, New Hampshire: *Cold Regions Research and Engineering Laboratory*, 14

- Semiletov, I.P. (1999). Aquatic sources and sinks of CO₂ and CH₄ in the polar regions. *Journal of the Atmospheric Sciences*, 56, 286-306
- Strayer, R.F., & Tiedje, J.M. (1978). In situ methane production in a small, hypereutrophic, hard-water lake: Loss of methane from sediments by vertical diffusion and ebullition. *Limnology and Oceanography*, 23, 1201-1206
- Ulaby, F.T., Moore, R.K., & Fung, A.K. (1986). *Microwave remote sensing: active and passive, Vol. I, Microwave Remote Sensing Fundamentals and Radiometry*, Addison-Wesley, 465
- Varadharajan, C. (2009). Magnitude and spatio-temporal variability of methane emissions from a eutrophic freshwater lake. *Ph.D. Thesis, Department of Civil and Environmental Engineering, Massachusetts Institute of Technology*, 243 pp
- Vas, D.A. (2010). Understanding the plumbing of methane ebullition seeps in interior Alaska thermokarst-lake sediments from high temporal resolution seep monitoring *MSc. Project Report, Water and Environmental Research Center, University of Alaska*, 90 pp.
- Walter Anthony, K.M., Vas, D.A., Brosius, L., Chapin III, F.S., Zimov, S.A., & Zhuang, Q. (2010). Estimating methane emissions from northern lakes using ice-bubble surveys *Limnology and Oceanography: Methods*, 8, 592-609
- Walter, K.M., Chanton, J.P., Chapin, F.S., Schuur, E.A.G., & Zimov, S.A. (2008a). Methane production and bubble emissions from arctic lakes: Isotopic implications for source pathways and ages. *Journal of Geophysical Research-Biogeosciences*, 113, G00A08
- Walter, K.M., Engram, M., Duguay, C.R., Jeffries, M.O., & Chapin, F.S. (2008b). The potential use of synthetic aperture radar for estimating methane ebullition from Arctic lake. *Journal of the American Water Resources Association*, 44, 305-315
- Walter, K.M., Smith, L.C., & Chapin, F.S. (2007). Methane bubbling from northern lakes: present and future contributions to the global methane budget. *Philosophical Transactions of the Royal Society a-Mathematical Physical and Engineering Sciences*, 365, 1657-1676
- Walter, K.M., Zimov, S.A., Chanton, J.P., Verbyla, D., & Chapin, F.S. (2006). Methane bubbling from Siberian thaw lakes as a positive feedback to climate warming. *Nature*, 443, 71-75
- Weeks, W.F., Fountain, A. G., Bryan, M. L., Elachi, C. (1978). Differences in Radar Return From Ice-Covered North Slope Lakes. *Journal of Geophysical Research*, 83, 4069-4073
- Weeks, W.F., Sellmann, P. , Campbell, W. J. (1977). Interesting features of radar imagery of ice covered north slope lakes. *Journal of Glaciology*, 18, 129-136

Whiting, G.J., & Chanton, J.P. (1993). Primary production control of methane emission from wetlands. *Nature*, 364, 794-795

Zimov, S.A., Voropaev, Y.V., Semiletov, I.P., Davidov, S.P., Prosiannikov, S.F., Chapin, F.S., Chapin, M.C., Trumbore, S., & Tyler, S. (1997). North Siberian lakes: A methane source fueled by Pleistocene carbon. *Science*, 277, 800-802

Zimov, S.A., Schuur, E.A.G., & Chapin, F.S. (2006). Permafrost and the global carbon budget. *Science*, 312, 1612-1613

Chapter 2 Estimating methane ebullition in thermokarst lakes with space-borne synthetic aperture radar (SAR)¹

2.1 Abstract

Northern high latitude wetlands and thermokarst lakes in permafrost regions have been identified as strong sources of methane (CH₄), a powerful greenhouse gas. Quantifying the spatial distribution and magnitude of CH₄ sources in these regions has become increasingly important in the current scenario of global warming and amidst concerns of partial release of the large permafrost soil carbon pool through thawing by thermokarst lakes. Ebullition (bubbling) is an important mode of CH₄ emission from thermokarst lakes to the atmosphere. However, due to its high spatial and temporal variability, large uncertainties remain in estimating the magnitude of ebullition emissions from lakes. Synthetic Aperture Radar (SAR) remote sensing of lake ice is a potentially valuable tool to constrain bottom-up estimates of lake ebullition in regions where lake ice forms. Here we tested various SAR imaging parameters as they correlate to field measurements of CH₄ ebullition bubbles in the ice of ten thermokarst lakes on the northern Seward Peninsula, Alaska. We found that ebullition bubbles trapped in frozen lakes were strongly correlated with L-band single polarized horizontal (HH) SAR ($R^2 = 0.70$, $P = 0.002$, $n = 10$) and with the 'roughness' component of a classic Pauli decomposition of PALSAR L-band quad-polarized signal ($R^2 = 0.77$, $P = 0.001$, $n = 10$). We found no such correlation with ERS-2

¹ Engram, M., Walter Anthony, K.M., Meyer, F., Grosse, G. Estimating methane ebullition in thermokarst lakes with space-borne synthetic aperture radar (SAR). Submitted to *Journal of Remote Sensing of Environment*.

C-band single polarized vertical (VV) SAR. We present the results of our single-pol and quad-pol SAR geospatial analysis, a discussion of probable scattering mechanisms of ebullition bubbles in frozen thermokarst lakes, and a recommendation for the optimal season for SAR observation of ebullition. Results of this study indicate that calibrated L-band SAR could be a valuable tool for estimating CH₄ ebullition in lakes on a regional scale by evaluating the backscatter intensity from early winter lake ice.

2.2 Introduction

Physical changes from the 0.65° C global temperature increase since the early twentieth century (Burroughs 2007) are evident in the Arctic, including retreating glaciers (Berthier et al. 2010), drastic reduction of multi-year sea ice and ice extent in the Arctic Ocean (Comiso et al. 2008), warming and thinning permafrost (Romanovsky et al. 2010) and broad changes in terrestrial environments (Hinzman et al. 2005). Complex feedbacks evolve from changes in these individual arctic system components, which may result in further acceleration of arctic warming (Higgins and Cassano 2009; Lawrence et al. 2008). Greenhouse gases (GHG), specifically methane (CH₄), are at the highest atmospheric concentrations ever recorded (Dlugokencky et al. 2009) and the highest in reconstructed atmospheric history (Chappellaz et al. 1993). CH₄ is a particularly powerful GHG, 25 to 28 times more effective at retaining heat in the atmosphere than carbon dioxide (CO₂) over a 100 year time horizon (Boucher et al. 2009). Yet the contributions from individual CH₄ sources to the atmosphere are not well determined and CH₄ emissions from lakes is currently missing from global CH₄ budgets (Bastviken et al. 2011; Chen and Prinn 2006; IPCC 2007).

Lakes produce a significant amount of CH₄ year round (Bastviken et al. 2004; Walter et al. 2006) as microbes decompose organic matter in many anaerobic lake bottom sediments. Although production rates increase with warmer substrate temperatures in lake beds (Duc et al. 2010) the primary driver of CH₄ production in lakes is the availability of organic substrates (Mazeas et al. 2009; Valentine et al. 1994). Thus, despite freezing air temperatures and ice covering the lake surface, methanogenesis continues in northern lake sediments during winter months, resulting in a large pulse of CH₄ to the atmosphere at spring ice melt (Huttunen et al. 2003; Phelps et al. 1998; Zimov et al. 1997).

Thermokarst lakes are especially productive in their CH₄ emissions owing to organic matter supplied by thawing permafrost (Walter et al. 2006). Thermokarst lakes are widespread in high latitude lowlands where long-term cold climates resulted in formation of perennially frozen ground (permafrost). Permafrost, defined by ground temperatures below 0 °C for more than two consecutive years, is found in about 24% of the northern hemisphere land surface (Zhang et al. 1999). In many arctic and subarctic regions permafrost consists of ground ice-rich sediments and soils containing large amounts of organic matter that accumulated over centuries to tens of millennia (Schirrmeister et al. 2011; Tarnocai et al. 2009). Climate change and surface disturbance since the Late Glacial period (beginning ca. 14.5 thousand years before present) resulted in massive and widespread degradation of permafrost and the formation of thermokarst lakes due to melt of ground ice, surface subsidence and positive feedbacks between topographic change, hydrology, and lake thermal regimes (Brosius et al. 2011; Grosse et al. 2011; Schirrmeister et al. 2011; Walter et al. 2007a). Today, an estimated 253,000 to 378,000 km² are covered with thermokarst lakes in ice-rich permafrost regions of the Arctic (Grosse et al. 2011).

In thermokarst lakes, CH₄ is created from the decomposition of ancient organic matter supplied as thawing permafrost releases carbon that was previously sequestered (Zimov et al. 1997). Methane emissions from thermokarst lakes constitutes a positive feedback in a continued global warming scenario: as temperature increases, more organic-rich permafrost will thaw, increasing CH₄ production, which will in turn contribute to higher atmospheric CH₄ concentrations and thus increased air temperatures (Walter et al. 2006).

Often, the primary mode of CH₄ emission from lakes is ebullition (Bastviken et al. 2011; Keller and Stallard 1994), whereby gas escapes lake bottom sediments and ascends as free state gas bubbles through the shallow water column to the lake surface. In Siberian thermokarst lakes, ebullition comprised 95% of total lake emissions (Walter et al. 2006).

Methane ebullition bubbles form distinctive patterns in winter lake ice when viewed from above, as they come to rest under lake ice, which rapidly thickens around them in early winter (Figure 2.1a). From a vertical (side) view (Figure 2.1b), ebullition bubbles have flattened tops and often exhibit tapered tips. Clusters of CH₄ bubbles trapped in ice usually range in size from centimeters to decimeters, but large ebullition point sources can generate clusters of bubbles with diameters that exceed one meter. Bubbles from point source ebullition seeps are stacked in ice that generally grows to over one meter thick in arctic lakes. Based on their ice-bubble patterns, size, and short term flux rates, Walter et al. (2006) categorized the ebullition seep bubble clusters into four distinct types corresponding to ebullition flux rates: Type A (lowest flux), Type B, Type C and Hotspots (highest flux). Long-term (up to 700 days) gas emission rates from each of these ebullition seep categories were measured on several Alaskan and Siberian lakes using underwater bubble traps anchored over point source CH₄ seeps (Walter Anthony et al. 2010). Since these

point-source ebullition seeps can dominate whole-lake CH₄ emissions in northern lakes, but are spatially heterogeneous across the lake surface (Walter Anthony and Anthony 2012; Wik et al. 2011), CH₄ emission flux measurements are often underestimated with floating roving traps. Stationary traps placed over discrete point-source seeps effectively measure CH₄ ebullition that roving traps tend to miss (Walter Anthony et al. 2010; Walter et al. 2006).

The magnitude of pan-arctic lake CH₄ emissions is unknown, and broad-scale estimates are highly variable (6-35 Tg CH₄ yr⁻¹) (Bastviken et al. 2011; Walter et al. 2007b). If lake CH₄ could be detected and quantified using remote sensing, then remote sensing could potentially help to constrain the current estimate of CH₄ emissions from lakes by providing regional synoptic-scale data of lake ice in early winter. Space-borne synthetic aperture radar (SAR), in particular, has high potential to provide such estimates.

SAR, an active sensor, is not dependent on solar illumination and can therefore image landscapes during dark arctic winters when lake ice forms. SAR uses microwave frequencies with wavelengths in the centimeter range that are long enough to penetrate clouds and dry snow covering lakes (Hall 1996). Microwave sensing from Side Looking Airborne Radar (SLAR) in the late 1970's (Mellor 1982) and subsequent studies using space-borne SAR to image lake ice (Duguay et al. 2002; Jeffries et al. 1994; Morris et al. 1995) have proven microwave backscatter to be sensitive to different types of freshwater ice with small (millimeter-scale) tubular gas bubbles in lake ice. SAR has been used to ascertain lake ice grounding (freezing to lake bed) to infer lake depth which determines water availability under ice in winter for fish habitat, ice road construction and rural domestic water sources (Duguay and Lafleur 2003; Jeffries et al. 1996; Kozlenko and Jeffries 2000). SAR determination of grounded lake ice versus floating ice assists

climate change assessments and the study of lake geomorphology (Arp et al. 2011). In a pilot study, C-band (5.6 cm wavelength) SAR single polarized horizontal (HH) backscatter values correlated with CH₄ ebullition bubble area and CH₄ flux on a small number of lakes in the northern foothills of Alaska's Brooks Range (Walter et al. 2008), showing the potential of space-borne SAR to quantify ebullition from frozen lakes on a regional scale.

The objectives of this study were to test and compare multiple types of satellite-based SAR to determine which SAR regime is most sensitive to the detection of centimeter-to-meter scale ebullition bubbles in lake ice, and to determine the scattering mechanism. First, we tested the hypotheses that one or both of C-band single polarized vertical (VV) SAR backscatter and L-band (23.6 cm wavelength) SAR backscatter will show a significant positive correlation with CH₄ ebullition bubbles in or under lake ice. Then, in order to separate and omit other non-bubble bright targets in lake ice, we investigated the mechanism of SAR scattering for layered CH₄ bubbles. We tested the hypothesis that a polarimetric decomposition of quad-polarized SAR data would show a significant positive correlation with CH₄ bubbles in or under lake ice with one or more of the decomposed signals: roughness, double-bounce or volumetric scattering. We discuss the possible explanations for this scattering mechanism and select the most likely phenomenon, as determined by differences in the dielectric constants of the gas, ice and water. Finally, we compared regression models of our study lakes in fall and spring to lay the groundwork for the future work of actually estimating regional-scale lake CH₄ emissions from SAR intensity through the inversion of a generalized regression model of SAR backscatter levels and ebullition.

2.3 Methods

2.3.1 Study site

We compared SAR values of lake ice to *in situ* field measurements of CH₄ bubbles trapped in the lake ice along transects on 10 lakes surveyed in late October and early November 2008 on the northern Seward Peninsula, Alaska (USA), near 66.53°N, 164.35°W (Figure 2.2). Here, thermokarst lakes formed in the continuous permafrost of icy, and organic-rich Pleistocene ‘yedoma’ loess soils (Höfle et al. 2000; Plug and West 2009). Lakes have degraded up to 75% of the permafrost in this region during the Holocene (Jones, M., et al. 2011). Thermokarst lakes in the study region are highly dynamic and had expansion rates of 0.35 – 0.39 m yr⁻¹ over the 1950-2007 period (Jones, B., et al. 2011). Methane seeps in yedoma-type thermokarst lakes cluster above baydjarakhs (Walter Anthony and Anthony 2012), which are conical thermokarst mounds with ~10 m spacing, consisting of thawed permafrost soils that remained in place as Pleistocene-aged ice wedges melted beneath the lakes. Study lakes were chosen to represent three different types of thermokarst lakes present on the northern Seward Peninsula: (1) relatively-deep lakes (depth of 2-10 m) with steep banks of yedoma permafrost, (2) shallow, large lakes (depth of 1-2 m) formed in lowlands over previously drained lake basins; and (3) lakes that straddle virgin yedoma and drained basins with both deep and shallow areas in their bathymetry. Study lakes size ranged from 11,000 m² to 784,000 m².

2.3.2 In-situ field measurements of CH₄ ebullition bubbles in lake ice

Transect locations for *in situ* CH₄ bubble surveys were selected in the context of the geomorphology of each lake. We chose transect sites near various high- and low-bluff

thermokarst shores to be representative of the different types of thermokarst activity in each lake. Other transect locations were chosen to represent the off-shore and center zones of the lake. We surveyed bubbles through the lake ice along 27 transects on ten lakes (Table 2.1). Bubble surveys were conducted following the methods of Walter Anthony et al. (2010) as described specifically for this site by Walter Anthony and Anthony (2012). Briefly, we shoveled snow off strips of lake ice one meter wide and 9 to 219 m long, categorizing the visible bubble clusters into four types (A, B, C, and Hotspot) that correspond to measured CH₄ flux values. We measured the length and width of each cluster and marked the location of clusters with a dual frequency differential global positioning system (DGPS) receiver (Leica 1230). Reference and roving receivers were used in the real-time kinematic mode (RTK) to obtain differentially-corrected positions in real time with positional errors of 0.5 to 1.5 cm (Figure 2.3). In order to provide a contrast for testing SAR sensitivity, we surveyed lakes that ranged from low to high with respect to ebullition bubble density. Transect locations were restricted on some lakes by the presence of opaque surface ice (white ice), which prevented visual bubble measurements. Since ebullition is a spatially variable phenomenon, by sampling with straight transects one can potentially walk between bubble clusters and under-sample ebullition. To mitigate this potential error in sampling, we shoveled snow and surveyed all seeps from a large, irregular polygon (625 m²) on a high-CH₄ emitting lake margin. Methane concentrations in ebullition bubbles (up to 86% CH₄) were determined using gas chromatography (Walter Anthony and Anthony 2012). In addition, we ignited gas trapped in ice bubble clusters as an *in situ* field test for the presence of elevated concentrations of CH₄ in bubbles.

2.3.3 Comparison of single-pol C-band and L-band SAR for detection of ebullition bubbles in lake ice

We investigated backscatter response in space-borne SAR from CH₄ bubbles in early winter lake ice using a variety of wavelengths, incidence angles, polarizations, and processing methods. To determine the type of SAR wavelength and polarization that is returned from CH₄ ebullition bubbles in and under lake ice, we evaluated single polarity SAR data with two different wavelengths: L-band data (23.6 cm) acquired by the Japan Aerospace exploration Agency's (JAXA) Advanced Land Observing Satellite's (ALOS) Phased-Array type L-band SAR (PALSAR) and C-band data (5.6 cm) from the European Remote Sensing Satellite 2 (ERS-2). Satellite data acquisition limitations prevented comparing data with two different wavelengths while at the same time holding all other signal parameters identical (incidence angle, polarization). Our comparison of wavelengths therefore included differences in wavelength, polarization and incidence angle. SAR data were obtained from the Alaska Satellite Facility (ASF) as calibrated, detected image products (Level 1.5) processed with restituted satellite ephemeris data. Scenes were post-processed with MapReady software (2.3.6) using the geocoding option to create geotiffs in UTM 3N, NAD83. The image intensities were scaled to decibel (dB) scale. Due to the limited quality of the satellite orbit information and the low quality of the topographic data available for our area of interest, the geolocation of the each image was additionally refined in ArcMap (9.3) using a lateral translation to fit each lake to perimeters as determined by reference data. We automated geoprocessor workflow with Python (2.5) scripting.

To determine lake perimeters needed for SAR registration, we refined the geolocation of a single nadir scene of the Panchromatic Remote-sensing Instrument for Stereo Mapping

(PRISM) sensor onboard the ALOS satellite. The PRISM nadir scene from Oct. 14, 2008, pixel size 2.5m, was rectified to orthorectified BELA (Bering Land Bridge National Preserve, National Park Service) 2003 aerial photos (Manley et al. 2007) obtained from the Geographic Information Network of Alaska (<http://www.gina.alaska.edu/>), using ice-wedge polygons as tie points (Jones et al. 2008). Again using lateral translation, this method shifted the most current image of changeable thermokarst lake shorelines to align with the most geospatially accurate reference data in a way that would not distort the shapes of the lakes. Lake perimeters were digitized in ArcMap (9.3).

All available ERS-2 and PALSAR Fine Beam Single polarization mode acquisitions from late October and early November 2008 were used in our analysis (Table 2.2). We used a single diagonal pixel distance (17.68 m) as a shoreline buffer to insure exclusion of bright land (Walter et al. 2008). Pixels farther than this specified distance from the lake shore were extracted, converted to power scale ($power\ scale = 10^{\left[\frac{\sigma^0}{10}\right]}$) then averaged for the whole-lake statistical analysis.

Mean SAR backscatter values for the entire lake, omitting shoreline buffer areas, were compared to the bubble area and ebullition flux along transects for nine of the ten study lakes. One small, shallow lake, Fox Den Lake, was omitted from the analysis because of a combination of small lake size, floating vegetation mats and seasonally and annually fluctuating water levels that periodically exposed large peaty mounds just below the water surface. One lake with high CH₄ ebullition near shore, but very low CH₄ ebullition in the center, Lake Claudi, was spatially segmented in ArcGIS into center and an outer lake zones, resulting in a sample size of 10 water bodies: 8 lakes plus the 2 zones from Lake Claudi (Table 2.1). Bubble area was calculated as the

sum of the area of all bubble clusters on transects divided by the total area surveyed on each lake. Ebullition seeps measured along transects were assumed to represent the distribution of ebullition seeps across the whole lake. For lakes with a high density of bubbles or a large number of survey transects, this is a reasonable assumption (Walter Anthony and Anthony 2012); however, ebullition is known to be a spatially heterogeneous process. We assigned flux values for each type of CH₄ seep using the seasonal data from the long-term data of Walter Anthony et al. (2010) set to estimate a fall (Sept. 1- Dec. 29) and spring (Feb. 1- May 30) CH₄ flux per square meter of transects.

2.3.4 Using Pauli decomposition of quad-pol L-band SAR to determine the scattering mechanism of ebullition bubbles associated with lake ice

In order to determine the mechanism of SAR scattering from CH₄ bubbles, we conducted a second analysis with fully polarized (quad-pol) L-band SAR from the ALOS PALSAR instrument. Due to scarcity of quad-pol PALSAR data acquisitions over the study site only few SAR data were available for this analysis (Table 2.3). Level 1.0 data were obtained from ASF and processed to single look complex (SLC) images using a custom processor including a radio frequency interference (RFI) notch filtering algorithm (Doulgeris and Meyer 2011; Meyer et al. 2011; Meyer et al. 2012) to create a Pauli decomposition (Cloude and Pottier 1996; Haijiang et al. 2009) that would be free from interference caused by long range ground radar defense installations near our study site.

In the Pauli decomposition, the full polarized scattering matrix of a SAR acquisition is expressed as the complex sum of a set of Pauli matrices, where an elementary scattering mechanism is associated for each basis matrix. In the monostatic case, where sender and receiver

are mounted on the same platform, the Pauli matrix basis can be reduced from originally four to three matrices whose determinants can be used to decompose the fully polarized SAR backscatter signal into three bands, which represent different types of classic scattering mechanisms: band 1 emphasizes 'double bounce'; band 2 shows 'volumetric scattering'; and band 3 includes predominantly 'single bounce' scattering (Figure 2.4). These interpretations are based on consideration of the properties of the Pauli matrices when they undergo a change of wave polarization base (Lee and Pottier 2009).

We compared all three bands from the Pauli decomposition to bubble area and to the fall or spring flux according to the acquisition dates of SAR scenes. GIS analysis methods were the same as those used for single-pol data: we used an ~18 m buffer distance to omit bright shore pixel contamination, then rectified the Pauli images with lateral translations in GIS for each lake. In portions of some lakes, we observed abrupt changes from light to dark pixels in portions of some lakes in sequential spring images. The pixels in the later images were 5-10 dB darker than in previous images and compared to surrounding ice. These lakes were omitted from the spring regression, under the assumption that this change to a dark SAR signature was an indicator of grounded ice, similar to the pattern observed with grounded ice in C-band SAR in previous studies (Duguay et al. 2002; Jeffries et al. 1994).

Statistical analysis consisted of least squares linear regression for four possible correlations: C-band SAR (VV) or L-band SAR (HH) vs. area of ice containing bubbles; and L-band SAR (Pauli decomposition) vs. area of ice containing bubbles and vs. CH₄ flux. We performed statistical analyses using SPSS software (16.0).

2.4 Results

2.4.1 Comparison of C-band and L-band SAR

Our investigation of two different SAR imaging modes, each from a different satellite, was designed to determine if either satellite's SAR wavelength or polarization configuration drives the interaction of microwave signals with CH₄ ebullition bubbles in early winter lake ice. C-band SAR data from ERS-2, with VV polarization, showed no correlation with the percentage of lake ice area that contained CH₄ bubbles (Figure 2.5a).

There were only two single polarized L-band scenes acquired in fall 2008, each with different incidence angles. L-band HH acquisitions on 9-Nov-2008 (8:53 UTC) and 11-Nov-2008 (8:36 UTC) both showed a positive correlation with CH₄ bubble area at the 95% confidence level (Figure 2.5b) (9-Nov-2008: $R^2 = 0.70$, $P = 0.002$; 11-Nov-2008: $R^2 = 0.71$, $P = 0.002$). There was a 3-6 dB higher signal from all lakes on the second date.

For both L-band HH and C-band VV SAR, backscatter increased over time: images from later dates showed brighter lake ice. However, lake ice with C-band VV SAR had higher backscatter than lake ice with L-band HH SAR image by 4-8 dB, when comparing images from the same date (Nov. 9th, 2008) (Figure 2.6). Higher backscatter from C-band VV SAR, compared to L-band HH SAR was not uniform over the entire image, but was particular to lake ice. Sigma-naught values from frozen lakes were as high or higher than backscatter from land in the 9-November C-band VV image, but were less than land backscatter values in the 9-November L-band image.

2.4.2 L-band SAR polarimetric decomposition

To obtain more information about the mechanism of scattering from CH₄ bubbles, we examined PALSAR L-band quad-polarized data that were processed using the Pauli decomposition. The positive correlation between field measured bubble area and Band 3 of the Pauli decomposition ($R^2 = 0.77$, $P < 0.001$) and the absence of correlation with Bands 1 and 2 indicates that the primary scattering mechanism of CH₄ bubbles associated with lake ice is single-bounce/roughness (Figure 2.7). Compared to correlations achieved with either of the originally observed single polarimetric channels (Figure 2.5b), the 'roughness' channel of a Pauli decomposition produced better absolute correlation coefficients with higher statistical significance and less residual scatter about the regression line (Figure 2.7).

All nine quad-polarized L-band SAR scenes that were acquired over the study site by PALSAR showed a positive correlation with ebullition bubble area. Acquisitions occurred in two time periods: fall (October and November) and spring (March and April). Three of the four fall scenes also showed a statistically significant positive correlation with the fall seep-flux at the 95% confidence level (Figure 2.8). While all of the spring scenes were positively correlated with the spring flux, only one was statistically significant using a 95% confidence level criterion (Figure 2.8a).

2.5 Discussion

2.5.1 C-band and L-band single-polarized SAR and CH₄

There are several possible explanations for failure of C-band ERS-2 to correlate with ebullition bubbles, despite the positive signal we observed with the L-band. SAR wavelength is

directly proportional to penetration ability: longer wavelengths penetrate farther into a medium (Ulaby et al. 1981). Wavelength size also determines the size of a target that can scatter the wave, depending on the type of scattering from the target, Raleigh or Mie scattering. One possible reason the shorter C-band did not correlate with either ebullition area or flux is that C-band may have been reflecting off other features in addition to ebullition bubbles, preventing isolation of the ebullition signal. It is possible that C-band could be reflecting off surface features, such as white ice or tissues of aquatic macrophytes frozen in lake ice, while the longer L-band penetrates these surface features.

Another potential problem with C-band VV SAR, is variations due to ice thickness. Leconte et al. (2009) performed a cold-room lab experiment using a C-band Continuous Wave Frequency Modulated (CW-FM) radar and inclusion-free ice with a smooth top (air/ice interface) and bottom (ice/water interface), using different incidence angles and radar polarizations. These controlled experiments demonstrated that C-band VV return from freshwater ice increases with ice thickness and were especially high with steep incidence angles of less than 30° , such as those used by ERS-2. In our study, high radar return from ice itself could have overshadowed any increased return caused by CH_4 bubbles in ERS-2 imagery.

Results from Leconte et al. (2009) also explain why we observed a positive correlation with C-band from RADARSAT-1 (R1) Standard Beam 3 SAR and ebullition bubbles in our pilot study (Walter et al., 2008), while we did not see a similar correlation with C-band ERS-2 SAR over the Seward Peninsula lakes in this study. ERS-2, with VV polarization and an average 23° degree incidence angle, did not show a correlation with ebullition bubbles. R1, which has HH polarization with a variable incidence angle and Standard 3 beam mode ($\sim 34^\circ$ incidence angle),

showed a correlation with CH₄ bubbles. In controlled laboratory conditions (Leconte et al. 2009), C-band radar backscatter measured from clear ice with a 23° incidence angle with VV polarization (ERS-2's parameters) was 11 dB higher than the radar return from a 34° incidence angle with HH polarization (R1 Standard 3 parameters). This high backscatter from clear, bubble-free ice from ERS-2 SAR probably overpowers any ebullition bubble signal, while R1's weaker response to clear ice could allow detection of a separate backscatter from ebullition bubbles.

While there are no similar controlled experiment results for L-band radar, an examination of SAR imagery shows that lake ice looks very different in C and L-bands. We found that lake ice in C-band VV images was brighter than surrounding land in early winter (Figure 2.5), while lake ice in L-band images remained darker than land until late spring. From such a delay in relative brightness we infer that L-band HH (21° - 34°) is less sensitive to ice thickening than is C-band VV (23°). Images from the same date in early winter show higher C-band sigma-naught values (-9 to -13 dB) than L-band (-17 to -19 dB). This is another indication that L-band is less sensitive to clear ice itself than C-band. This observation corroborates that a large part of the C-band VV 23° SAR backscatter signal from winter lakes is caused by the ice itself, not by bubbles. This conclusion is in accordance with Jeffries et al. (1994), who noted the continuous rise in backscatter with ice formation, despite discrete layering of clear ice on top of tubular-bubble rich ice. Such layers should cause a stair-stepped SAR increase if increased backscatter were caused by gas bubbles alone, either in or under the ice. This C-band VV 23° response to ice crystals in thickening lake ice appears to overshadow any weaker bubble signal.

2.5.2 Utility of L-band single-polarized SAR as an indicator of ebullition

The fact that both L-band single-pol (HH) SAR scenes showed a significant positive correlation with area of CH₄ bubbles in lake ice (Figure 2.5b) indicates that L-band SAR has the potential to be a useful tool in detecting and quantifying CH₄ ebullition in lakes. While additional ice thickness could explain part of the higher backscatter from the later image, temperatures were relatively mild (with an average for the three days of -8 °C), indicating slow ice growth. The magnitude of the difference in the regression models for two scenes that were just two days apart (Figure 2.5b) indicates a driver other than two additional days of ice formation. One possible explanation for the difference in backscatter in the two single polarized SAR scenes is that these acquisitions had different incidence angles (34° and 21°) which may interact with CH₄ bubbles or with clear ice differently. Further investigation using scenes of single-pol L-band SAR with the identical incidence angles could help assess the utility of single-pol L-band for quantifying CH₄.

Another possible explanation for the large difference in backscatter observed over only two days at the same sites is the potential increases in ebullition activity in the lakes on these dates. Abrupt changes in the rate of ebullition are known to occur over time scales of hours to days as a result of changes in atmospheric pressure (FechnerLevy and Hemond 1996; Kellner et al. 2006; Mattson and Likens 1990; McQuaid and Mercer 1991; Rosenberry et al. 2003; Strack et al. 2005; Tokida et al. 2007). A period of high pressure preceded the Nov. 9 image; however an abrupt drop in atmospheric pressure occurred on Nov. 10 and 11. We cannot rule out the possibility that the higher backscatter on Nov. 11 was the result of an atmospheric-pressure induced increase in the quantity of ebullition bubbles trapped under ice on this date. Clearly

more research is needed to improve understanding of the causes of variability in the single-pol L-band SAR responses over time.

2.5.3 Scattering mechanisms

Using a Pauli polarimetric decomposition, we can derive conclusions about the actual scattering mechanism that defines the signature of a surface feature in a SAR image. Band 3 of a Pauli decomposition, which indicates roughness as the scattering mechanism (Haijiang et al. 2009), showed a significant correlation with both ebullition area and flux, while no significant correlations with Band 1, (double bounce) or Band 2 (volumetric scattering) were found. This indicates that the dominant mechanism of scattering of ebullition bubbles is ‘roughness’, rather than volumetric or double-bounce. We expect that this ‘roughness’ signal is caused by CH₄ bubbles collecting under the ice surface (Figure 2.4). The presence of CH₄ ebullition bubbles trapped beneath the bottom surface of the lake ice creates a large dielectric contrast at the gas/water interface ($\epsilon'_{\text{H}_2\text{O}_{0.1^\circ\text{C}_{1.27\text{GHz}}} \approx 88$, $\epsilon'_{\text{CH}_4} \approx 1$) (Meissner and Wentz 2004; Skolunov 1997). As bubbles come to rest under the ice, a new scattering interface is created since bubbles change the effective under-ice topography, increasing surface roughness due to their irregular pattern and the varying shape over time (Figure 2.4). Our data support this hypothesis: the strong relationship observed between the SAR roughness component and ebullition bubble area (Figure 2.7) may be explained by the positive relationship between the quantity of bubbles trapped under ice and the dielectric contrast observed as a result in SAR.

As well as providing insight into the CH₄ bubble-related mechanism of scattering, another reason for applying a Pauli decomposition before geophysical data analysis is that the regressions for Pauli were statistically stronger than for single-pol L-band SAR. A statistically stronger

regression model is a more useful tool for estimating CH₄ flux from SAR backscatter through inversion of the linear model.

2.5.4 Seasonal variability of the Pauli decomposition SAR signal and implications for CH₄ detection

Regression lines with Pauli 'roughness' component and CH₄ flux calculated for both spring and fall acquisitions clustered into a lower fall group and higher spring group (Fig. 2.8), a separation probably caused by seasonal ice and bubble conditions. L-band SAR, while not as sensitive to freshwater ice crystals as C-band SAR, is reflected to a small extent by clear ice. Thicker lake ice in spring may reflect more of L-band energy back to the satellite than in fall and could be expressed by the higher Pauli DN (y-intercept) found in the spring regression model.

Another potential reason for disparate fall and spring regression models is the different physical attributes of ebullition bubbles in these seasons, caused by seasonal changes in ice-growth rates. Lake ice grows faster in the fall and more slowly in the spring since latent heat must be conducted upward through existing ice in order for new ice to form (Duguay et al. 2003). As ice thickens, it inhibits heat flux from water below, providing insulation from colder air temperatures. Where present, snow can act as an additional layer of insulation. In fall, some sub-ice ebullition bubbles are smaller than spring bubbles due to thin fast-growing ice that quickly surrounds and traps bubbles to keep them separated and small. Slower-growing spring ice allows more time for some bubbles to merge into larger bubbles, as they accumulate under ice. These seasonal differences in bubble volume accumulation rates would be expected for some ebullition seep types, such as high-flux Type C and hotspot seeps, which have been shown to have relatively constant ebullition rates among seasons (Walter Anthony et al. 2010).

Fall appears to be the more conducive season for detecting and quantifying lake CH₄ ebullition with SAR for several reasons. Some lakes freeze to the bottom in the spring causing significantly lower backscatter values and a darker appearance in images than floating ice (Jeffries et al. 1994; Mellor 1982; Weeks et al. 1977). The low backscatter from grounded ice is a confounding factor when estimating CH₄ emissions using SAR brightness. Particularly in this study, after omitting lakes with plummeting sigma-naught values in spring scenes, the decrease in the number of lakes considered for a regression probably deflated the statistical significance of the R² values (Figure 2.8). In addition to grounded ice (frozen to lake bottom) in spring/late winter scenes, SAR backscatter can also be decreased if liquid water pools on the lake surface during spring melt. Liquid water from melting of surface snow and ice causes a low SAR backscatter signal due to specular reflection away from a monostatic sensor. Another reason to prefer fall over spring for CH₄ estimation with SAR is that lake ice reaches its maximum thickness in spring (Duguay et al. 2002; Jeffries et al. 1994). While it seems that L-band reflects less from clear ice itself, thinner ice in the fall can reduce the L-band SAR backscatter from clear ice, allowing for greater sensitivity to CH₄ bubbles.

2.5.5 Factors that could confound the SAR signal from ebullition bubbles

In addition to ice thickness itself, several other factors could confound the CH₄ ebullition SAR signal. 'White ice' is an opaque surface present as the top layer of ice on some lakes. It is caused by snow and slush during freezing conditions and is well documented in SAR and lake ice literature (Jeffries et al. 1996; Jeffries and Sackinger 1990; Morris et al. 1995; Walter et al. 2008). We recorded the presence of white ice on the lakes in our study area as part of our field survey protocol. Since white ice forms differently each year, yet we observed consistent regression

models from year to year in fall, when white ice was a relatively thin layer (<10 cm) where it occurred, white ice did not seem to be a large confounding factor with L-band SAR in this study.

Another factor that could affect the accuracy of SAR vs. ebullition bubbles is the accuracy of our field-based estimates of lake ebullition. Walter Anthony and Anthony (2012) demonstrated that the uncertainty of CH₄ flux estimates based on ice bubble ground survey transects is greatest for lakes with low seep density and least for lakes with high seep density. The more closely-grouped the bubbles, the more likely a linear transect is to accurately represent the spatial distribution of CH₄ bubbles for the entire lake.

Aquatic plants frozen in lake ice could also reflect SAR and cause a brighter return that could be confused with backscatter caused by CH₄ bubbles under lake ice. Macrophytes, growing in known locations on the Seward Peninsula study lakes, were visibly very bright in X-band images of the lake ice, visibly noticeable in C-band images, but were not visible in L-band SAR. Unlike the shorter wavelengths of C and X bands, the longer wavelength of L-band SAR could allow penetration of vegetation in lake ice, just as L-band penetrates the vegetation canopy in terrestrial scenes (Brown et al. 1992; Lu 2007; Ranson and Sun 1994). While further study could conclusively determine if any additional increase in L-band SAR backscatter is caused from plants frozen in the ice, we saw no evidence of higher outlying points in any of the L-band regression analyses from our few Seward Peninsula study lakes with known plants colonies.

2.6 Conclusions

This study shows that L-band SAR backscatter positively correlates with CH₄ ebullition bubbles in or under lake ice on thermokarst lakes in the northern Seward Peninsula, Alaska. This statistically significant relationship exists not only for the physical bubble area, as measured

along transects on the ice, but also for 120-day fall CH₄ flux values. Further work to investigate the relationship between ebullition bubbles and L-band SAR should include the creation of one statistical regression model that could be inverted to estimate CH₄ flux from a SAR image of lake ice. SAR L-band imagery could then be a valuable tool to provide an approximate estimation of CH₄ ebullition flux in northern lakes on a regional scale.

2.7 Acknowledgements

We thank L. Plug, C. Arp, L. Oxtoby, L. Farquharson, B. Jones, and A. Strohm for assistance with field data collection; L. Plug for collecting and processing DGPS field data; and R. Daanen for coordination with Ice Alaska. We thank CH2M Hill Polar Services (CPS) for field logistics during our 2008 fall field campaign. We thank D. Verbyla for his assistance with Python scripts for GIS. We acknowledge the Alaska Satellite Facility (ASF), both the NASA's Distributed Data Archive Center and JAXA's (Japan Aerospace exploration Agency's) Americas ALOS Data Node for access to SAR data, M. Harbin and ASF's User Services Office for assistance with data ordering and satellite tasking; ASF's User Tool Development group for MapReady image software and fast action in resolving software issues; W. Albright for expert consultation in obscure SAR documentation of peak-to-side-lobe ratios. We thank A. Dulgeris for polarimetric assistance. We thank to D. Podrasky, J. Geck, B. Truessel, K. Morris and D. Verbyla for invaluable assistance with manuscript review and editing. Access to field sites on the Bering Land Bridge National Preserve was granted by the National Parks Service (permit # BELA-2008-SCI-0002).

Role of the funding sources: Funding was provided by NASA Carbon Cycle Sciences NNX08AJ37G and NNX11AH20G and NSF IPY #0732735. The present work represents solely the opinion of the authors and no one from the funding agencies was involved in study design, collection, analysis and interpretation of the data, and in the writing of the publication.

2.8 References

- Arp, C.D., Jones, B.M., Urban, F.E., & Grosse, G. (2011). Hydrogeomorphic processes of thermokarst lakes with grounded-ice and floating-ice regimes on the Arctic coastal plain, Alaska. *Hydrological Processes*, 25, 2422-2439
- Bastviken, D., Cole, J., Pace, M., & Tranvik, L. (2004). Methane emissions from lakes: Dependence of lake characteristics, two regional assessments, and a global estimate. *Global Biogeochemical Cycles*, 18, Gb4009
- Bastviken, D., Tranvik, L.J., Downing, J.A., Crill, P.M., & Enrich-Prast, A. (2011). Freshwater Methane Emissions Offset the Continental Carbon Sink. *Science*, 331, 50-50
- Berthier, E., Schiefer, E., Clarke, G.K.C., Menounos, B., & Remy, F. (2010). Contribution of Alaskan glaciers to sea-level rise derived from satellite imagery. *Nature Geoscience*, 3, 92-95
- Boucher, O., Friedlingstein, P., Collins, B., & Shine, K.P. (2009). The indirect global warming potential and global temperature change potential due to methane oxidation. *Environmental Research Letters*, 4, 044007
- Brosius, L.S., Walter Anthony, K.M., Grosse, G., Chanton, J.P., Farquarson, L.M., Overduin, P.P., & Meyer, H. (2011). Using δD of permafrost melt water to constrain thermokarst lake contributions to atmospheric CH_4 during the last deglaciation. *Journal of Geophysical Research - Biogeosciences*, In review
- Brown, R.J., Manore, M.J., & Poirier, S. (1992). Correlations between X-band, C-band, and L-band imagery within an agricultural environment. *International Journal of Remote Sensing*, 13, 1645-1661
- Burroughs, W.J. (2007). *Climate Change: A Multidisciplinary Approach*. Cambridge University Press, 392
- Chappellaz, J., Blunier, T., Raynaud, D., Barnola, J.M., Schwander, J., & Stauffer, B. (1993). Synchronous changes in atmospheric CH_4 and Greenland climate between 40-KYR and 8-KYR BP. *Nature*, 366, 443-445
- Chen, Y.H., & Prinn, R.G. (2006). Estimation of atmospheric methane emissions between 1996 and 2001 using a three-dimensional global chemical transport model. *Journal of Geophysical Research-Atmospheres*, 111, D10307
- Cloude, S.R., & Pottier, E. (1996). A review of target decomposition theorems in radar polarimetry. *Ieee Transactions on Geoscience and Remote Sensing*, 34, 498-518
- Comiso, J.C., Parkinson, C.L., Gersten, R., & Stock, L. (2008). Accelerated decline in the Arctic Sea ice cover. *Geophysical Research Letters*, 35, L01703

- Dlugokencky, E.J., Bruhwiler, L., White, J.W.C., Emmons, L.K., Novelli, P.C., Montzka, S.A., Masarie, K.A., Lang, P.M., Crotwell, A.M., Miller, J.B., & Gatti, L.V. (2009). Observational constraints on recent increases in the atmospheric CH₄ burden. *Geophysical Research Letters*, *36*, L18803
- Dougeris, A.P., & Meyer, F.J. (2011). Severe Radio Frequency Interference in ALOS PALSAR Imagery. *Proceedings of the 5th International Workshop on Science and Applications of SAR Polarimetry and Polarimetric Interferometry (POLinSAR 2011)*, Frascati, Italy, Special Publication of the European Space Agency SP-695, 8
- Duc, N.T., Crill, P., & Bastviken, D. (2010). Implications of temperature and sediment characteristics on methane formation and oxidation in lake sediments. *Biogeochemistry*, *100*, 185-196
- Duguay, C.R., Flato, G.M., Jeffries, M.O., Menard, P., Morris, K., & Rouse, W.R. (2003). Ice-cover variability on shallow lakes at high latitudes: model simulations and observations. *Hydrological Processes*, *17*, 3465-3483
- Duguay, C.R., & Lafleur, P.M. (2003). Determining depth and ice thickness of shallow sub-Arctic lakes using space-borne optical and SAR data. *International Journal of Remote Sensing*, *24*, 475-489
- Duguay, C.R., Pultz, T.J., Lafleur, P.M., & Drai, D. (2002). RADARSAT backscatter characteristics of ice growing on shallow sub-Arctic lakes, Churchill, Manitoba, Canada. *Hydrological Processes*, *16*, 1631-1644
- FechnerLevy, E.J., & Hemond, H.F. (1996). Trapped methane volume and potential effects on methane ebullition in a northern peatland. *Limnology and Oceanography*, *41*, 1375-1383
- Grosse, G., Jones, B., Arp, C. (in press, 2012). Thermokarst lakes, drainage, and drained basins. In: Shroder J (Editor in Chief), Giardino R, Harbor J (Eds.): *Treatise on Geomorphology*. Elsevier Academic Press, San Diego, CA, vol.8.
- Haijiang, W., Qihong, H., & Yiming, P. (2009). Polarization decomposition with S and T matrix of a PolSAR image. In, *ICCCAS 2009. International Conference on Communications, Circuits and Systems, 2009*. (pp. 530-532)
- Hall, D.K. (1996). Remote sensing applications to hydrology: Imaging radar. *Hydrological Sciences Journal-Journal Des Sciences Hydrologiques*, *41*, 609-624
- Higgins, M.E., & Cassano, J.J. (2009). Impacts of reduced sea ice on winter Arctic atmospheric circulation, precipitation, and temperature. *Journal of Geophysical Research-Atmospheres*, *114*, D16107

- Hinzman, L.D., Bettez, N.D., Bolton, W.R., Chapin, F.S., Dyrurgerov, M.B., Fastie, C.L., Griffith, B., Hollister, R.D., Hope, A., Huntington, H.P., Jensen, A.M., Jia, G.J., Jorgenson, T., Kane, D.L., Klein, D.R., Kofinas, G., Lynch, A.H., Lloyd, A.H., McGuire, A.D., Nelson, F.E., Oechel, W.C., Osterkamp, T.E., Racine, C.H., Romanovsky, V.E., Stone, R.S., Stow, D.A., Sturm, M., Tweedie, C.E., Vourlitis, G.L., Walker, M.D., Walker, D.A., Webber, P.J., Welker, J.M., Winker, K., & Yoshikawa, K. (2005). Evidence and implications of recent climate change in northern Alaska and other arctic regions. *Climatic Change*, 72, 251-298
- Höfle, C., Edwards, M.E., Hopkins, D.M., Mann, D.H., & Ping, C.-L. (2000). The Full-Glacial Environment of the Northern Seward Peninsula, Alaska, Reconstructed from the 21,500-Year-Old Kitluk Paleosol. *Quaternary Research*, 53, 143-153
- Huttunen, J.T., Alm, J., Saarijarvi, E., Lappalainen, K.M., Silvola, J., & Martikainen, P.J. (2003). Contribution of winter to the annual CH₄ emission from a eutrophied boreal lake. *Chemosphere*, 50, 247-250
- IPCC (2007). Climate Change 2007: The Physical Science Basis. Contribution of Working Group I to the Fourth Assessment Report of the Intergovernmental Panel on Climate Change. Cambridge Univ. Press, New York (Ed.)
- Jeffries, M.O., Morris, K., & Liston, G.E. (1996). A method to determine lake depth and water availability on the north slope of Alaska with spaceborne imaging radar and numerical ice growth modelling. *Arctic*, 49, 367-374
- Jeffries, M.O., Morris, K., Weeks, W.F., & Wakabayashi, H. (1994). Structural and stratigraphic features and ERS-1 synthetic-aperture radar backscatter characteristics of ice growing on shallow lakes in NW Alaska, winter 1991-1992. *Journal of Geophysical Research-Oceans*, 99, 22459-22471
- Jeffries, M.O., & Sackinger, W.M. (1990). Ice island detection and characterization with airborne synthetic aperture radar. *Journal of Geophysical Research-Oceans*, 95, 5371-5377
- Jones, B.M., Grosse, G., Arp, C.D., Jones, M.C., Anthony, K.M.W., & Romanovsky, V.E. (2011). Modern thermokarst lake dynamics in the continuous permafrost zone, northern Seward Peninsula, Alaska. *Journal of Geophysical Research-Biogeosciences*, 116, G00M03
- Jones, B.M., Hinkel, K.M., Arpi, C.D., & Eisner, W.R. (2008). Modern Erosion Rates and Loss of Coastal Features and Sites, Beaufort Sea Coastline, Alaska. *Arctic*, 61, 361-372
- Jones, M., Grosse, G., Jones, B.M., & Walter Anthony, K.M. (2012). Peat accumulation in a thermokarst-affected landscape in continuous ice-rich permafrost, Seward Peninsula, Alaska. *In review, Journal of Geophysical Research - Biogeosciences*
- Keller, M., & Stallard, R.F. (1994). Methane emission by bubbling from Gatun Lake, Panama. *Journal of Geophysical Research-Atmospheres*, 99, 8307-8319

- Kellner, E., Baird, A.J., Oosterwoud, M., Harrison, K., & Waddington, J.M. (2006). Effect of temperature and atmospheric pressure on methane (CH₄) ebullition from near-surface peats. *Geophysical Research Letters*, 33, L18405
- Kozlenko, N., & Jeffries, M.O. (2000). Bathymetric mapping of shallow water in thaw lakes on the North Slope of Alaska with spaceborne imaging radar. *Arctic*, 53, 306-316
- Lawrence, D.M., Slater, A.G., Tomas, R.A., Holland, M.M., & Deser, C. (2008). Accelerated Arctic land warming and permafrost degradation during rapid sea ice loss. *Geophysical Research Letters*, 35, L11506
- Leconte, R., Daly, S., Gauthier, Y., Yankielun, N., Bérubé, F., & Bernier, M. (2009). A controlled experiment to retrieve freshwater ice characteristics from an FM-CW radar system. *Cold Regions Science and Technology*, 55, 212-220
- Lee, J.-S., & Pottier, E. (2009). *Polarimetric Radar Imaging: From Basics to Applications*. CRC Press Taylor & Francis Group, Boca Raton, Fl., p. 214-215
- Lu, Z. (2007). ALOS PALSAR Interferometric Synthetic Aperture Radar (InSAR). *Alaska Satellite Facility News and Notes*, 4, 2
- Manley, W.F., Sanzone, D.M., Lestak, L.R., & Parrish, E.G. (2007). High-Resolution Orthorectified Imagery from 2003 for the Coastal Areas of Bering Land Bridge NP (BELA) and Cape Krusenstern NM (CAKR), Northwest Alaska. In: Fairbanks, AK: National Park Service, Arctic Network Inventory and Monitoring Program
- Mattson, M.D., & Likens, G.E. (1990). Air Pressure and Methane Fluxes *Nature*, 347, 718-719
- Mazeas, O., von Fischer, J.C., & Rhew, R.C. (2009). Impact of terrestrial carbon input on methane emissions from an Alaskan Arctic lake. *Geophysical Research Letters*, 36, L18501
- McQuaid, J., & Mercer, A. (1991). Air-pressure and methane fluxes. *Nature*, 351, 528-528
- Meissner, T., & Wentz, F.J. (2004). The complex dielectric constant of pure and sea water from microwave satellite observations. *IEEE Transactions on Geoscience and Remote Sensing*, 42, 1836-1849
- Mellor, J. (1982). Bathymetry of Alaskan Arctic Lakes: A key to resource inventory with remote sensing methods. *Ph.D. Thesis, Institute of Marine Science, University of Alaska*, 342 pp
- Meyer, F. J., Nicoll, J. B., Doulgeris, A. P. (2011). Characterization and Extent of Randomly-Changing Radio Frequency Interference in ALOS PALSAR Data. *Geoscience and Remote Sensing Symposium (IGARSS), 2011 IEEE International, Vancouver, Canada*. 2448-2451.
- Meyer, F. J., Nicoll, J., Doulgeris, A. P. (2012). Characterization and Correction of Residual RFI Signatures in Operationally Processed ALOS PALSAR Imagery. *Proceedings of EUSAR'12 Conference, 2012, Nurnberg, Germany*, accepted for publication.

- Morris, K., Jeffries, M.O., & Weeks, W.R. (1995). Ice processes and growth history on Arctic and sub-arctic lakes using ERS-1 SAR data. *Polar Record*, 31, 115-128
- Phelps, A.R., Peterson, K.M., & Jeffries, M.O. (1998). Methane efflux from high-latitude lakes during spring ice melt. *Journal of Geophysical Research-Atmospheres*, 103, 29029-29036
- Plug, L.J., & West, J.J. (2009). Thaw lake expansion in a two-dimensional coupled model of heat transfer, thaw subsidence, and mass movement. *Journal of Geophysical Research-Earth Surface*, 114, F01002
- Ranson, K.J., & Sun, G.Q. (1994). Mapping biomass of a northern forest using multifrequency SAR data. *IEEE Transactions on Geoscience and Remote Sensing*, 32, 388-396
- Romanovsky, V.E., Smith, S.L., & Christiansen, H.H. (2010). Permafrost thermal state in the polar Northern Hemisphere during the international polar year 2007-2009: a synthesis. *Permafrost and Periglacial Processes*, 21, 106-116
- Rosenberry, D.O., Glaser, P.H., Siegel, D.I., & Weeks, E.P. (2003). Use of hydraulic head to estimate volumetric gas content and ebullition flux in northern peatlands. *Water Resources Research*, 39, 1066
- Schirrmeister, L., Grosse, G., Wetterich, S., Overduin, P.P., Strauss, J., Schuur, E.A.G., & Hubberten, H.-W. (2011). Fossil organic matter characteristics in permafrost deposits of the northeast Siberian Arctic. *J. Geophys. Res.*, 116, G00M02
- Skolunov, A.V. (1997). Frequency-temperature curve of the complex dielectric constant and refractive index of water. *Fibre Chemistry*, 29, 367-373
- Strack, M., Kellner, E., & Waddington, J.M. (2005). Dynamics of biogenic gas bubbles in peat and their effects on peatland biogeochemistry. *Global Biogeochemical Cycles*, 19, GB2003
- Tarnocai, C., Canadell, J.G., Schuur, E.A.G., Kuhry, P., Mazhitova, G., & Zimov, S. (2009). Soil organic carbon pools in the northern circumpolar permafrost region. *Global Biogeochemical Cycles*, 23, GB2023
- Tokida, T., Miyazaki, T., Mizoguchi, M., Nagata, O., Takakai, F., Kagemoto, A., & Hatano, R. (2007). Falling atmospheric pressure as a trigger for methane ebullition from peatland. *Global Biogeochemical Cycles*, 21, GB2003
- Ulaby, F.T., Moore, R.K., & Fung, A.K. (1981). *Microwave remote sensing: active and passive, Vol. I, Microwave Remote Sensing Fundamentals and Radiometry*, Addison-Wesley, 465
- Valentine, D.W., Holland, E.A., & Schimel, D.S. (1994). Ecosystem and physiological controls over methane production in northern wetlands. *Journal of Geophysical Research-Atmospheres*, 99, 1563-1571
- Walter Anthony, K.M., & Anthony, P. (2012, in review). Constraining spatial variability of methane ebullition in thermokarst lakes using point-process models. *In review, Journal of Geophysical Research – Biogeosciences*

- Walter Anthony, K.M., Vas, D.A., Brosius, L., Chapin III, F.S., Zimov, S.A., & Zhuang, Q. (2010). Estimating methane emissions from northern lakes using ice-bubble surveys *Limnology and Oceanography: Methods*, 8, 592-609
- Walter, K.M., Edwards, M.E., Grosse, G., Zimov, S.A., & Chapin, F.S. (2007a). Thermokarst lakes as a source of atmospheric CH₄ during the last deglaciation. *Science*, 318, 633-636
- Walter, K.M., Engram, M., Duguay, C.R., Jeffries, M.O., & Chapin, F.S. (2008). The potential use of synthetic aperture radar for estimating methane ebullition from Arctic lake. *Journal of the American Water Resources Association*, 44, 305-315
- Walter, K.M., Smith, L.C., & Chapin, F.S. (2007b). Methane bubbling from northern lakes: present and future contributions to the global methane budget. *Philosophical Transactions of the Royal Society a-Mathematical Physical and Engineering Sciences*, 365, 1657-1676
- Walter, K.M., Zimov, S.A., Chanton, J.P., Verbyla, D., & Chapin, F.S. (2006). Methane bubbling from Siberian thaw lakes as a positive feedback to climate warming. *Nature*, 443, 71-75
- Weeks, W.F., P. Sellmann, W. J. Campbell (1977). Interesting features of radar imagery of ice covered north slope lakes. *Journal of Glaciology*, 18, 129-136
- Wik, M., Crill, P.M., Bastviken, D., Danielsson, A., & Norback, E. (2011). Bubbles trapped in arctic lake ice: Potential implications for methane emissions. *Journal of Geophysical Research-Biogeosciences*, 116, G03044
- Zhang, T., Barry, R.G., Knowles, K., Heginbottom, J.A., & Brown, J. (1999). Statistics and characteristics of permafrost and ground ice distribution in the Northern Hemisphere 1. *Polar Geography*, 23, 132-154
- Zimov, S.A., Voropaev, Y.V., Semiletov, I.P., Davidov, S.P., Prosiannikov, S.F., Chapin, F.S., Chapin, M.C., Trumbore, S., & Tyler, S. (1997). North Siberian lakes: A methane source fueled by Pleistocene carbon. *Science*, 277, 800-802

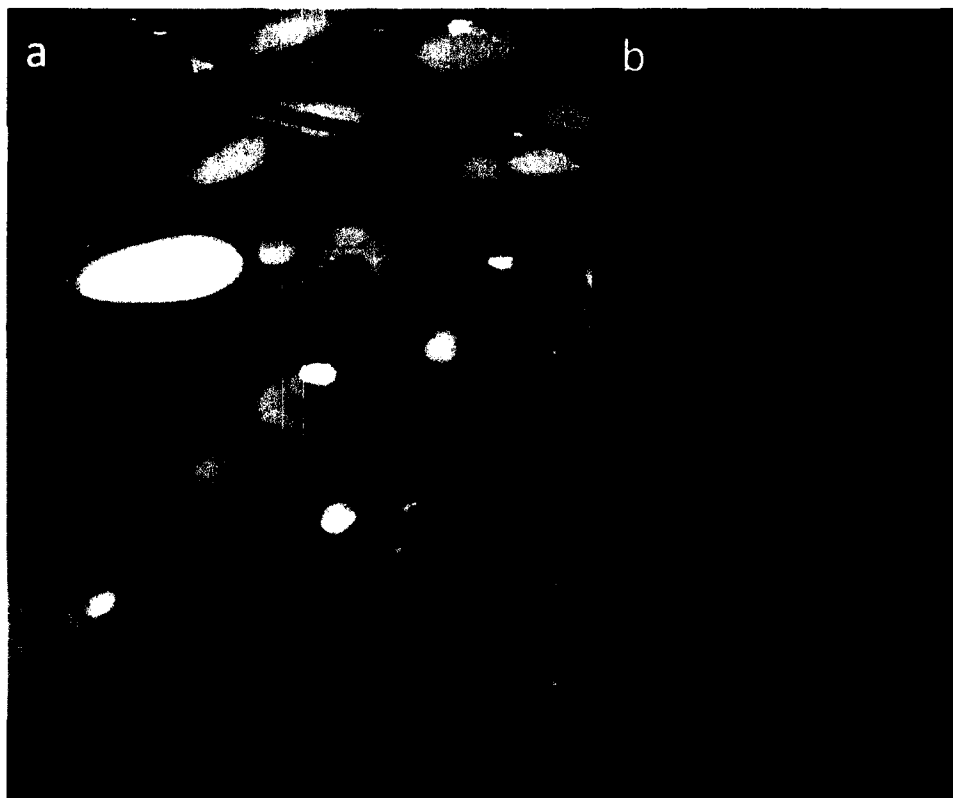


Figure 2.1: a) Example of a CH_4 ebullition bubble cluster trapped in ice on a thermokarst lake, as seen from top of ice and, b) vertical profile of ebullition bubbles, as seen from the side, in a block of clear lake ice. Bubbles frozen in ice commonly have conical shapes with large diameter of the cone facing up. This flattened top is formed as a bubble comes to rest under the lake ice sheet. The pointed tip at the bottom forms as ice freezes around the bubble, squeezing the gas into a point. Clear ice between bubbles indicates a duration of time passing without ebullition. Closely stacked bubbles indicate frequent ebullition events.

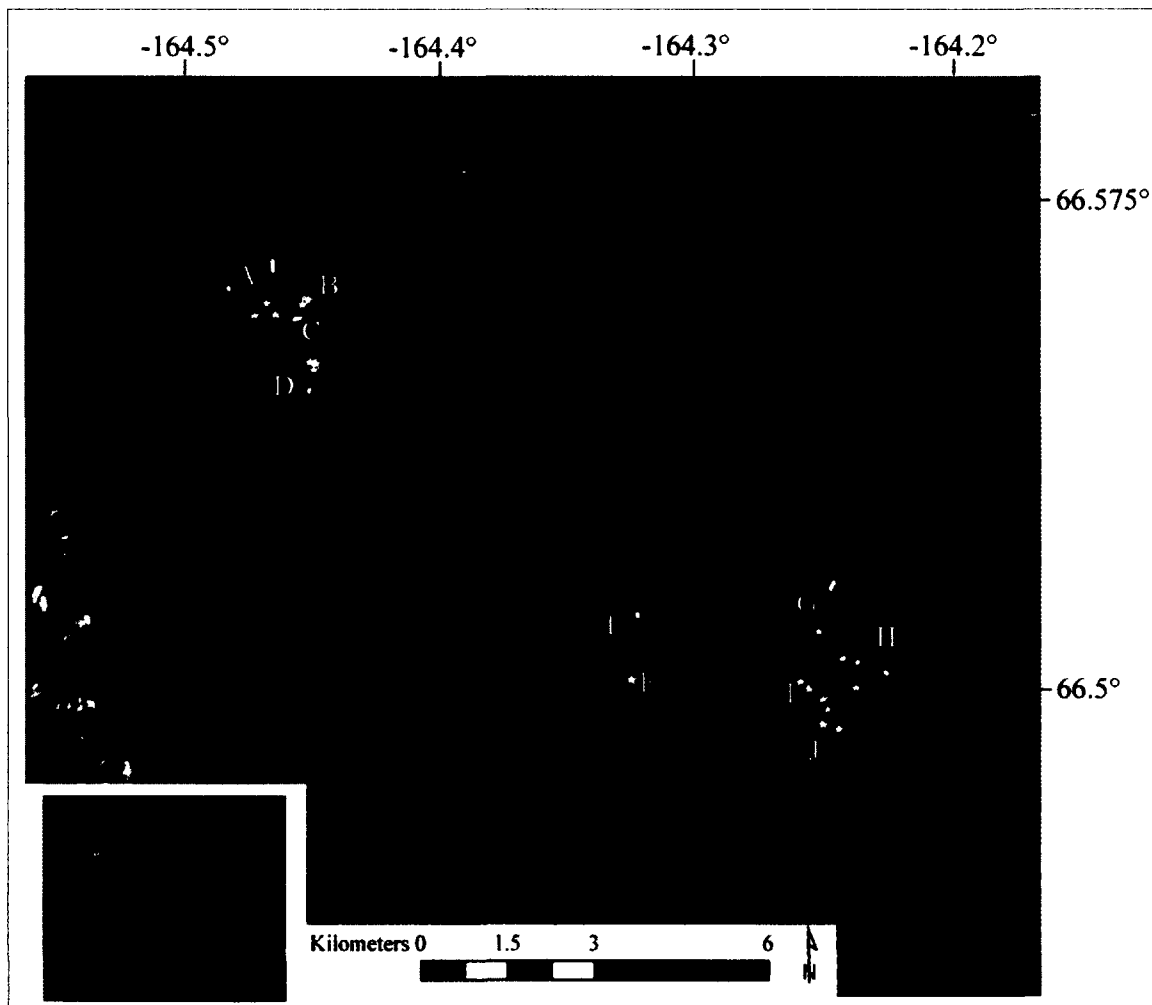


Figure 2.2: Study lakes on the thermokarst lake landscape of the northern Seward Peninsula, Alaska, USA. The scarred, mottled appearance in this Landsat TM composite image from the Geographic Information Network of Alaska (GINA) shows a thermokarst lake cycle that has been active since early Holocene. Dark, water filled lakes often overlap lighter, vegetation filled drained lake basins. White stars indicate location of bubble survey transects on early winter lake ice on lake margins with steep shores of yedoma permafrost. Non-starred white lines are locations of transects on shallow lowland margins. Lake names are A) Rhonda Lake, B) Cocker Gap Lake, C) Fox Den Lake, D) Lake Claudi, E) Island Lake, F) Tea Lake, G) Kim Lake, H) Owl Lake, I) Jaeger Lake, and J) Three Loon Lake.

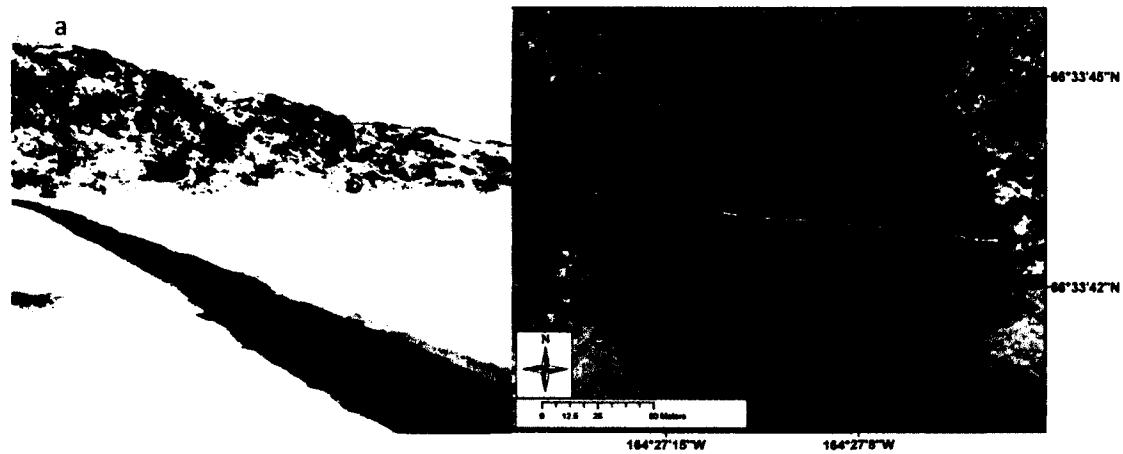


Figure 2.3: Methane bubble survey transect on a thermokarst lake as seen a) looking to the west while taking field measurements of size, type and location of bubble clusters through early fall lake ice; b) in GIS with DGPS points showing the location of CH₄ seeps with an orthorectified photo reference data (2003) as background.

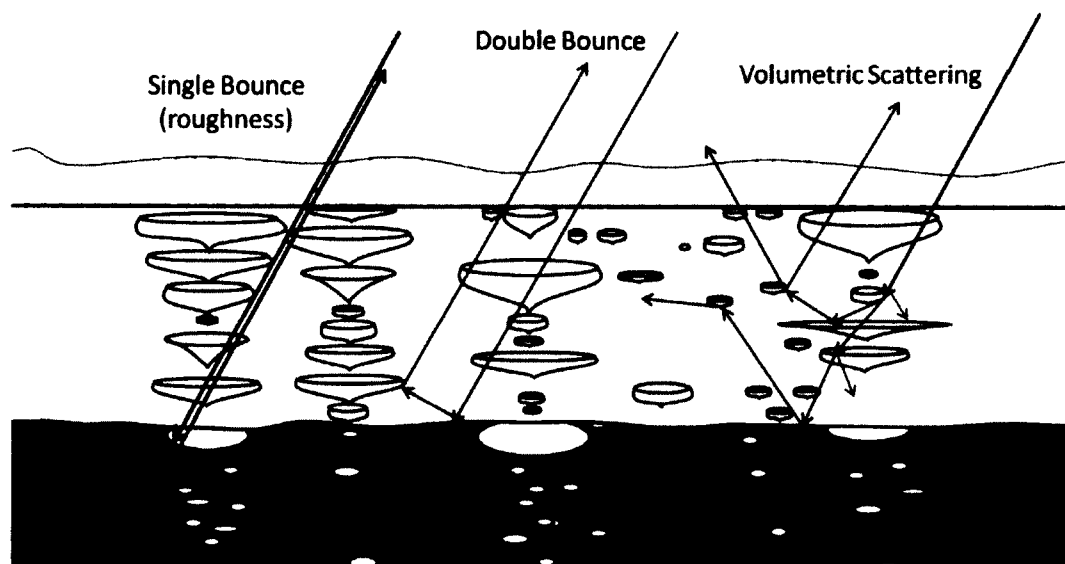
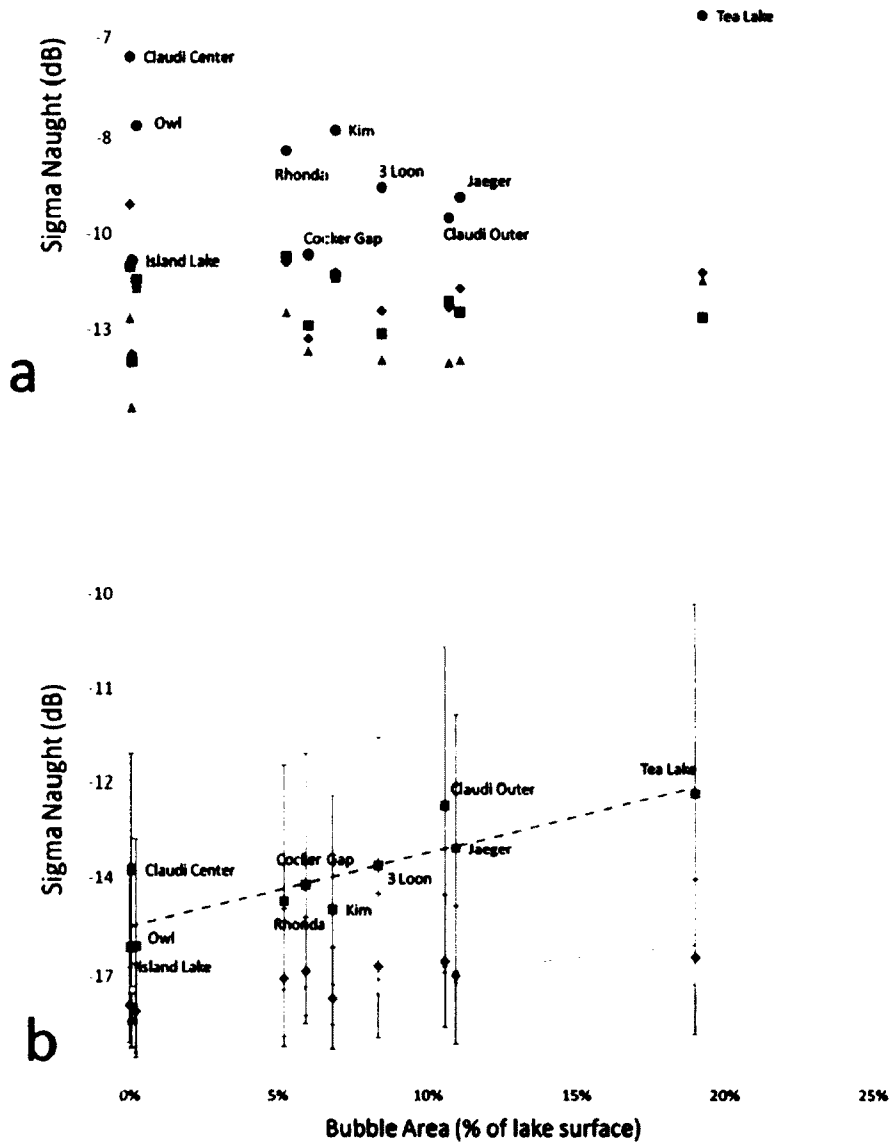


Figure 2.4: Pauli decomposition of fully-polarized SAR allows direct inference as to the scattering mechanism of a target. Classic SAR scattering mechanisms as they could apply to lake ice: single-bounce (roughness), double-bounce and volumetric scattering. Our analysis revealed that the single-bounce component of the Pauli decomposition showed a positive correlation with ebullition bubbles. This schematic, depicting snow (grey stars) on top of lake ice with ebullition bubbles over lake water (grey), with some bubbles ascending in the water column and some resting under the ice, shows the most probable single-bounce interface as indicated by arrows: from ebullition bubbles resting under lake ice. The real components of the dielectric constant (ϵ') for L-band radar frequencies are: $\epsilon' \approx 1$ for gas, $\epsilon' \approx 3.2$ for ice and, $\epsilon' \approx 88$ for cold water in the liquid phase.



Panel Symbol	Date	Incidence angle	Regression equation	R ²	Regression statistics, SPSS
b diamonds	Nov. 9, 2008	~34°	powerscale = 0.0672*(% bubble area) - 0.0135	0.711	P = 0,002
b square	Nov. 11, 2008	~21°	powerscale = 0.1534*(% bubble area) - 0.0302	0.705	P = 0,002

Figure 2.5: Comparison of single-polarized data from dates close to field measurements in fall 2008. a) C-band SAR (~23° incidence angle, VV polarization, ERS-2) backscatter from lake ice is not correlated with bubble area. Triangles represent values from Oct. 27th, grey squares from Nov. 9th, black diamonds from Nov. 12th, and circles from Nov. 15th. b) L-band SAR (HH, ALOS PALSAR) lake ice backscatter shows significant correlation with the percent of area of lake ice with bubbles. Error bars are +/- one standard deviation.

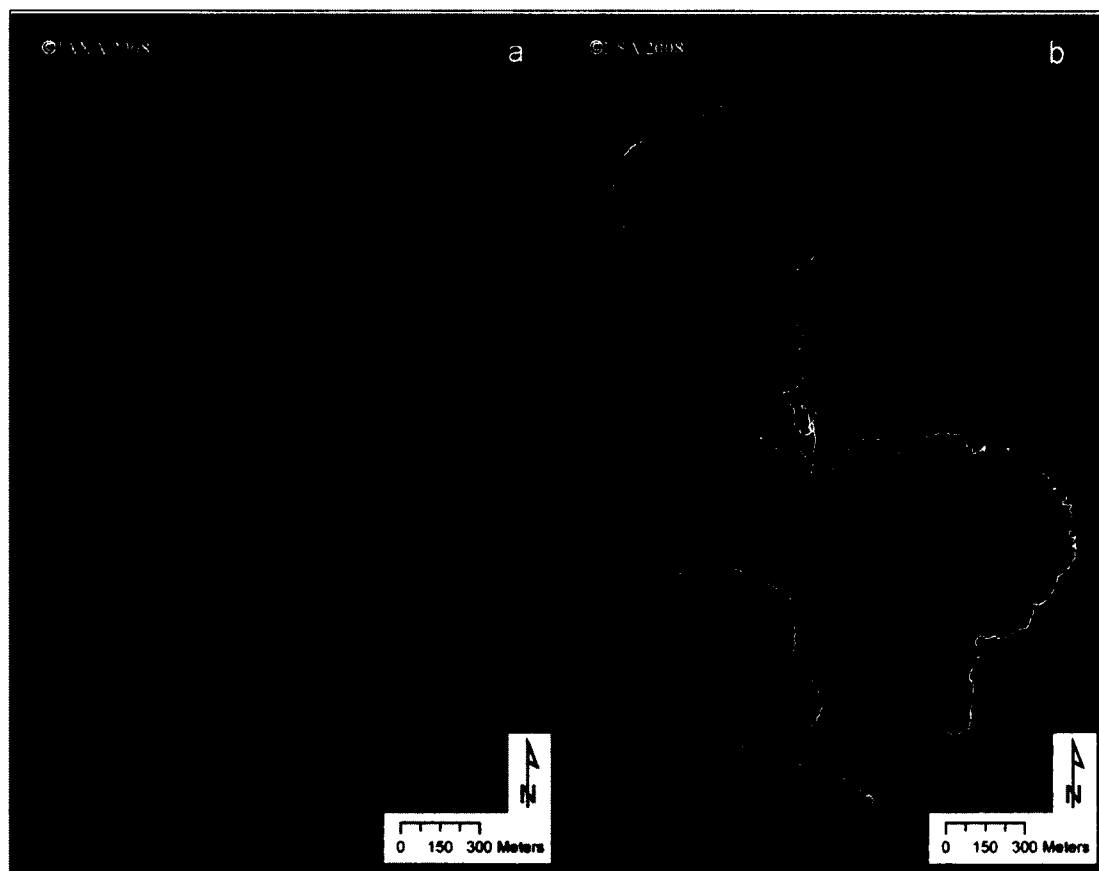


Figure 2.6: Comparison of same day 9-November-2008 SAR images a) L-band (23.6 cm wavelength) and b) C-band (5.6 cm wavelength). Lake ice in the C-band image is much brighter overall and brighter than the land in some cases. Lakes are outlined in white in the C-band image to distinguish lake ice from land.

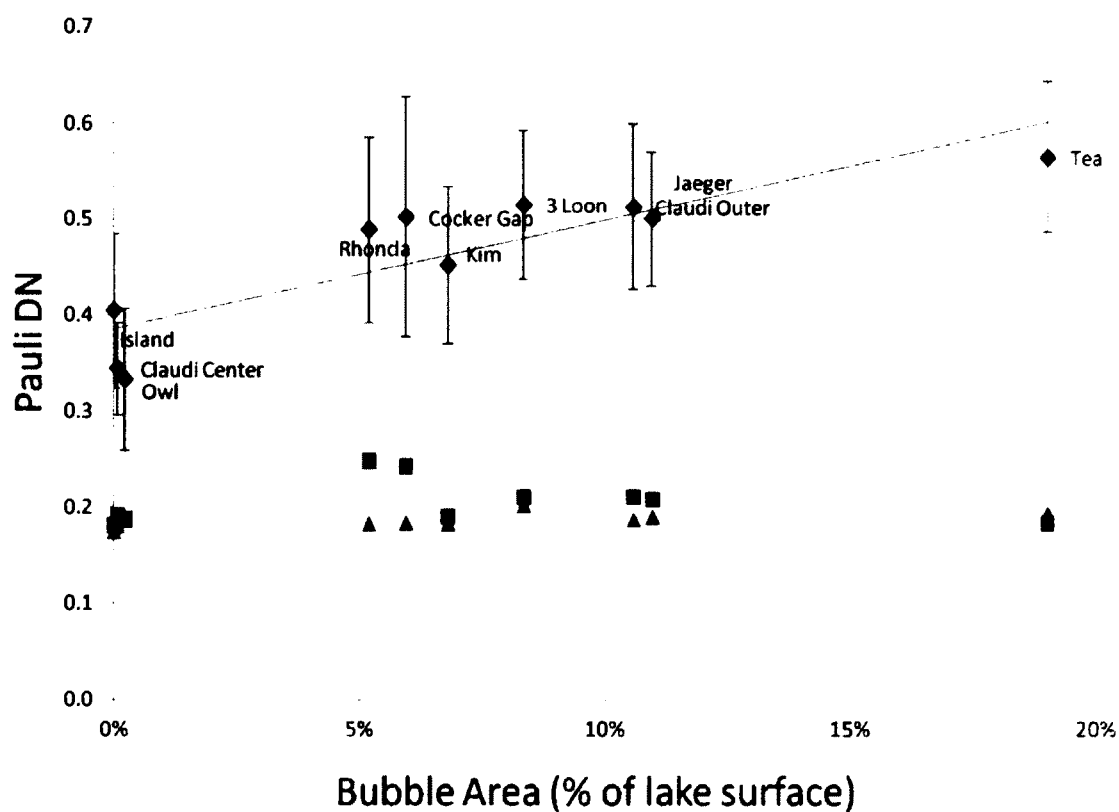


Figure 2.7: Significant positive correlation between single-bounce (roughness) from polarimetric decomposition of L-band quad-polarized data for Nov. 14, 2009 and percent of area of ice showing CH₄ ebullition, as measured in fall 2008. Diamonds show Pauli Band 3 (roughness), ~21° incidence angle; regression equation is Pauli DN = 1.1392*(% bubble area) + 0.3855, R² = 0.771, p = 0.001. Squares show Pauli Band 2 (volumetric scattering) and triangles show Pauli Band 1 (double bounce), neither of which show a correlation with percent of area of lake ice with ebullition bubbles. Error bars are +/- one standard deviation.

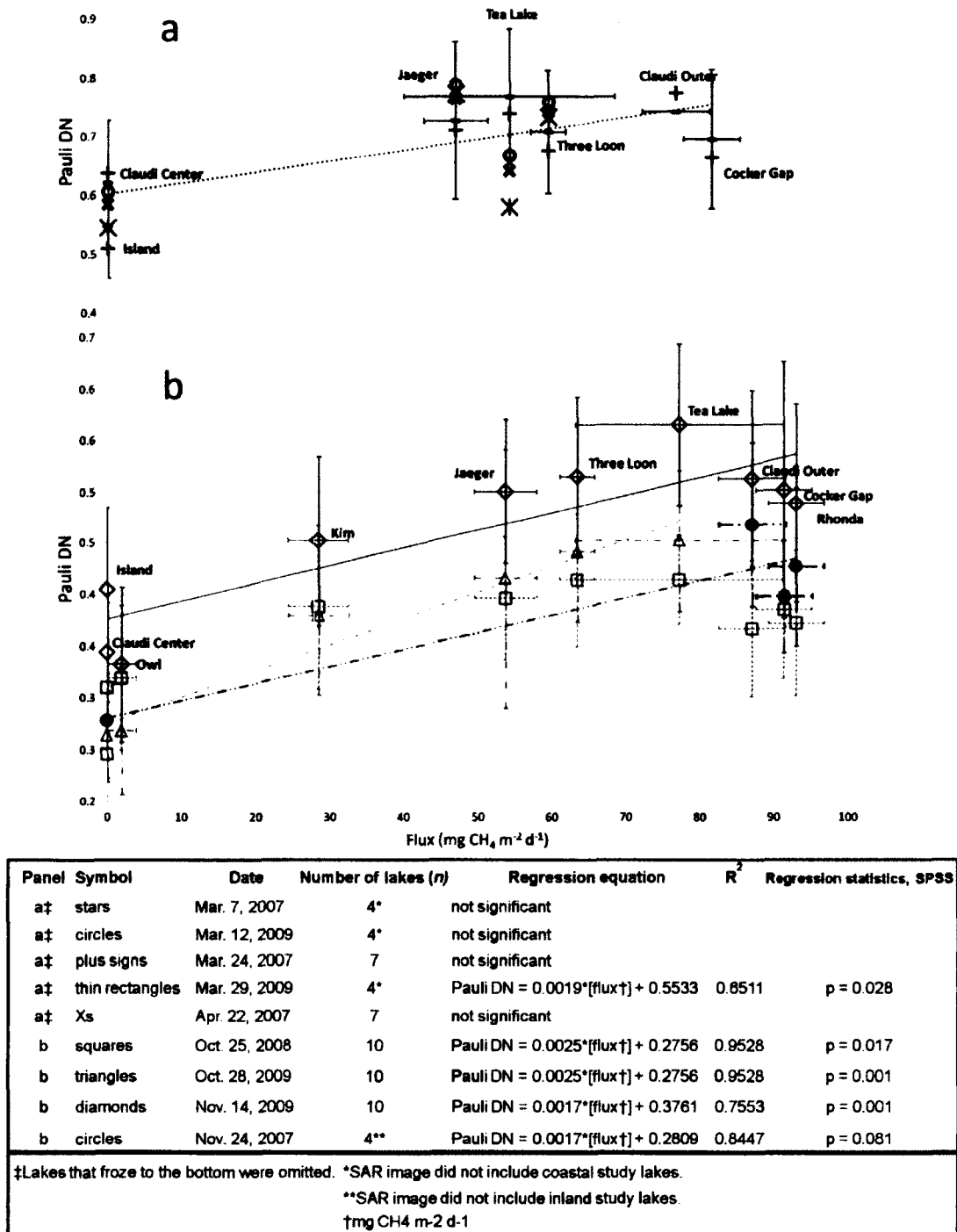


Figure 2.8: Pauli Band 3 roughness component of L-band PALSAR quad-polarized SAR backscatter from thermokarst lake ice, plotted against long-term (120 day) seasonal CH₄ flux for a) spring and b) fall. Error bars show +/- one standard deviation. Note different scales with higher spring SAR values.

Table 2.1: Methane ebullition bubble clusters identified in bubbles surveys along transects on early winter lake ice on the northern Seward Peninsula, Alaska, USA.

Lake name	Date bubble survey	Number of bubble clusters	Transect area (m ²)	Bubble Area (%)
Jaeger Lake	24-Oct-2008	942	394.9	10.94
Three Loon Lake	25-Oct to 26-Oct-2008	257	210.6	8.33
Island Lake	27-Oct-2008	0	21.6	0.00
Tea Lake	27-Oct-2008	127	20.0	19.00
Kim Lake	29-Oct-2008	322	164.0	6.79
Owl Lake	30-Oct-2008	51	146.2	0.22
Rhonda Lake	1-Nov to 6-Nov-2008	466	350.1	5.20
Cocker Gap Lake	2-Nov to 3-Nov-2008	368	201.9	5.94
Fox Den Lake	3-Nov-2008	136	92.1	5.04
Lake Claudi (outer)	3-Nov-2008	1783	775.9	10.57
Lake Claudi (inner)	19-Apr-2009	2	48.5	0.07

Table 2.2: SAR data used in single polarity geospatial analysis.

Date	Band	Incidence		Beam		
		Angle (θ)	Platform	Mode	Polarization	Geometry
OCT-27-2008	C-band	23°	ERS-2	STD	VV	descending
NOV 09 2008	C-band	23°	ERS-2	STD	VV	ascending
NOV-12-2008	C-band	23°	ERS-2	STD	VV	descending
NOV-15-2008	C-band	23°	ERS-2	STD	VV	descending
NOV-09-2008	L-band	34.3°	Palsar on ALOS	FBS	HH	ascending
NOV-11-2008	L-band	21.5°	Palsar on ALOS	FBS	HH	ascending

Table 2.3: List of PALSAR fully polarized data (HH, VV, HV and VH) used for analysis with Pauli decomposition. All data were acquired with an incidence angle of 21.5°.

Fall		Spring	
Date	Geometry	Date	Geometry
NOV-24-2007 22:18	descending	MAR-07-2007 08:35	ascending
OCT-25-2008 08:33	ascending	MAR-24-2007 08:37	ascending
OCT-28-2009 08:36	ascending	APR-22-2007 08:35	ascending
NOV-14-2009 08:39	ascending	MAR-12-2009 08:35	ascending
		MAR-29-2009 08:37	ascending

Chapter 3 General Conclusion

Measured bubble area of CH₄ ebullition bubbles trapped by lake ice and the associated CH₄ flux correlate with the 'roughness' component of a standard Pauli polarimetric decomposition of L-band quad-pol SAR. Early winter (fall) is the most advantageous time to use SAR to quantify these bubbles, since lake ice has not yet frozen to the bottom of shallow lake beds, a phenomenon known to dramatically decrease SAR backscatter.

Further investigation in SAR and CH₄ ebullition flux should include developing one regression model for L-band SAR, inverting the model to predict the amount of CH₄ trapped by ice on a lake, then validating that prediction with field measurements. If successful, this research will lead to developing region-scale maps of CH₄ ebullition flux from SAR data.

Other knowledge gaps associated with CH₄ ebullition flux, if filled, could also improve lake-source CH₄ estimates. These are not necessarily questions to be addressed with remote sensing. Do ebullition seeps appear to be static year after year? Are stationary point-source seeps observed only in northern lakes? What is the variability of the concentration of CH₄ compared to the total volume of gas emitted in an ebullition event? How does the availability and quality of organic matter in the substrate affect methanogenesis in relation to temperature? How is surface air pressure correlated with ebullition activity over various time scales? Finally, quantifying lake CH₄ emissions is important for input in the development of regional and global atmospheric CH₄ budgets.

Appendix A. Report on physical configuration of some types of methane (CH₄) ebullition bubbles in and under lake ice

Introduction

To provide insight into how physical shapes of CH₄ bubbles in and under lake ice influence synthetic aperture radar (SAR) radar reflectivity measurements, field studies to characterize bubbles were conducted on several lakes in April 2010.

Biogenic CH₄ produced in northern lake sediments rises to the surface via ebullition from irregularly spaced, temporally sporadic point-source seeps in lake sediments. Once the lake is frozen in early winter, CH₄ ebullition bubbles come to rest under the sheet of surface lake ice. Their shape is determined by the formation of congelation ice around them as lake ice thickens and the bubbles become encased. Ebullition bubbles trapped by lake ice produce an increased backscatter response from monostatic space-borne SAR instruments using certain imaging parameters.

Shape, size and spatial distribution of CH₄ ebullition bubbles frozen in and trapped under lake ice are dependent on the rate of gas emission into the water column. Walter et al. (2006) defined four distinct ebullition seep classes that can be identified by bubble presentations as seen through early winter lake ice from the top of the ice: A, kotenok; B, koshka; C, kotara, and Hotspot. Each of the four types of bubble clusters have been assigned an average CH₄ flux, as determined from long-term flux and CH₄ concentration measurements using stationary bubble traps on different Alaskan and Siberian lakes (Walter Anthony et al. 2010).

Here, I report on 1) the shape, size and spatial distribution of a fifth bubble category, the type 'N' (no flux) bubble class (PALIMMN), 2) the shape of type 'A' ebullition bubbles as

viewed from the side, 3) circular and non-circular patterns in medium flux type 'B' bubbles, as viewed from the top (horizontal spacing) and 4) previously undocumented ridges in the ice cavities created by bubbles in the two larger bubble classes, type 'C's and 'Hotspots'.

Shape, size and spacing of type 'N' bubble

Ebullition bubbles in lake ice that exhibit no vertical layering indicate a one-time event of gas emission, in contrast to bubbles that are vertically stacked, which indicate an episodic or periodic gas flux over time. This presentation of one single bubble or one layer of horizontally distributed bubbles with no vertical stacking of bubbles (Figure A.1) has been categorized as a Type 'N' (Walter, 2008, personal communication). Type 'N' bubbles represent lower gas emissions and likely comprise some of the 'background bubbling' reported by Walter et al. (2006). While Type 'N' conservatively does not receive an associated flux value, this class is consistently recorded during ice bubble surveys and has the potential to affect SAR backscatter. The size of Type 'N' bubbles is variable, from <1 cm to >30 cm, generally 0.5 cm to 15 cm in diameter. The top of type 'N' bubbles is flat, with a conical or lenticular shape when viewed from side profile. Horizontal spacing (when viewed from the top) is variable.

Shape of Type 'A' bubbles in vertical profile

Walter et al. (2006) has defined type 'A' ebullition bubbles as small distinct vertically layered bubbles that show separation in ice when viewed from top. Fewer than half of the bubbles can be merged laterally for the cluster to qualify as a type 'A'. The sizes of the clusters are

generally less than 50 cm in horizontal diameter. Although it rarely occurs, type 'A' bubbles may also be seen as a single isolated column of small bubbles instead of clustered in a group. Type 'A' bubbles have the lowest gas flux among the four types (Walter Anthony et al. 2010; Walter et al. 2006).

Ice separates layers of bubbles at their edges, although some of the bubbles can be joined vertically (Figure A.2, Figure A.3). From the side view the top of a bubble is flat, formed as the bubble hits the underside of the lake ice. Edges are usually rounded, sloping from the flat disk of the top surface and bulging to a slightly larger diameter, then tapering to a cone-shaped or a lens-like shape toward the bottom of the bubble.

Type 'B' patterns from horizontal profile

Type 'B' bubbles, as defined by Walter et al. (2006, 2008) are formed above CH₄ seeps with a higher flux than Type 'A' seeps. Individual bubbles trapped in ice within the cluster are generally 10-40 cm per bubble in length, and may have different widths depending on how the bubbles merge and spread out under the ice. The diameter of B-type bubble clusters is typically 20-70 cm. Bubbles often appear in round or elliptical cluster patterns with elongated curved bubbles surrounding a central point (Figure A.4). Individual B-bubbles are larger than Type 'A' and generally have an asymmetric shape (Figure A.5) as the result of joining two or more round bubbles.

Ridges formed in large bubble ice cavities.

From high-flux seeps, bubbles can coalesce into one large bubble under the ice around which new ice grows as the lake ice thickens. The large bubbles create cavities in the ice. Common structural features in the walls of these large cavities are stair-stepped ridges in the ice, each step formed as a new bubble joins the bottom of the bubble stack under the ice. Ridges are a function of how fast or slowly the ice forms in relation to large flux ebullition activity. Common ridge dimensions are 1 cm x 1 cm or 2cm x 2cm (Figure A.6).

Appendix A References

- Jones, B.M., Hinkel, K.M., Arp, C.D., & Eisner, W.R. (2008). Modern Erosion Rates and Loss of Coastal Features and Sites, Beaufort Sea Coastline, Alaska. *Arctic*, 61, 361-372
- Manley, W.F., Sanzone, D.M., Lestak, L.R., & Parrish, E.G. (2007). High-Resolution Orthorectified Imagery from 2003 for the Coastal Areas of Bering Land Bridge NP (BELA) and Cape Krusenstern NM (CAKR), Northwest Alaska.. Fairbanks, AK: National Park Service, *Arctic Network Inventory and Monitoring Program*
- PALIMMN. Pan-Arctic Lake-Ice Methane Monitoring Network (2010), last retrieved March 29, 2012. <<http://ine.uaf.edu/werc/palimmn/>>
- Walter Anthony, K.M., Vas, D.A., Brosius, L., Chapin III, F.S., Zimov, S.A., & Zhuang, Q. (2010). Estimating methane emissions from northern lakes using ice-bubble surveys *Limnology and Oceanography: Methods*, 8, 592-609
- Walter, K.M., Engram, M., Duguay, C.R., Jeffries, M.O., & Chapin, F.S. (2008). The potential use of synthetic aperture radar for estimating methane ebullition from Arctic lake. *Journal of the American Water Resources Association*, 44, 305-315
- Walter, K.M., Zimov, S.A., Chanton, J.P., Verbyla, D., & Chapin, F.S. (2006). Methane bubbling from Siberian thaw lakes as a positive feedback to climate warming. *Nature*, 443, 71-75

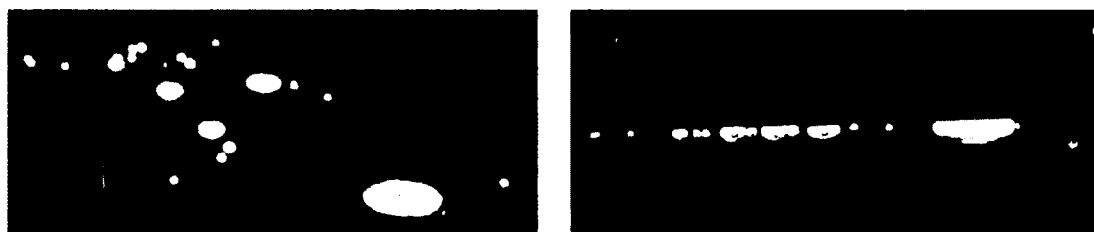
Appendix A Figures

Figure A.1: Type 'N' CH₄ bubbles viewed from top with slightly oblique viewing angle (a), and the same bubble group from side profile (b). Notice flat tops of bubble with circular shape, curved bulging sides, tapering to a lens shape or a conical shape at bottom of bubble. Type 'N' bubbles have no vertical layers and are formed when bubbles are released as a single event, not repeated regularly on time scales of days to weeks. The vertical striations in the image are an artifact of cutting ice blocks with a saw. Photos by M. Engram.

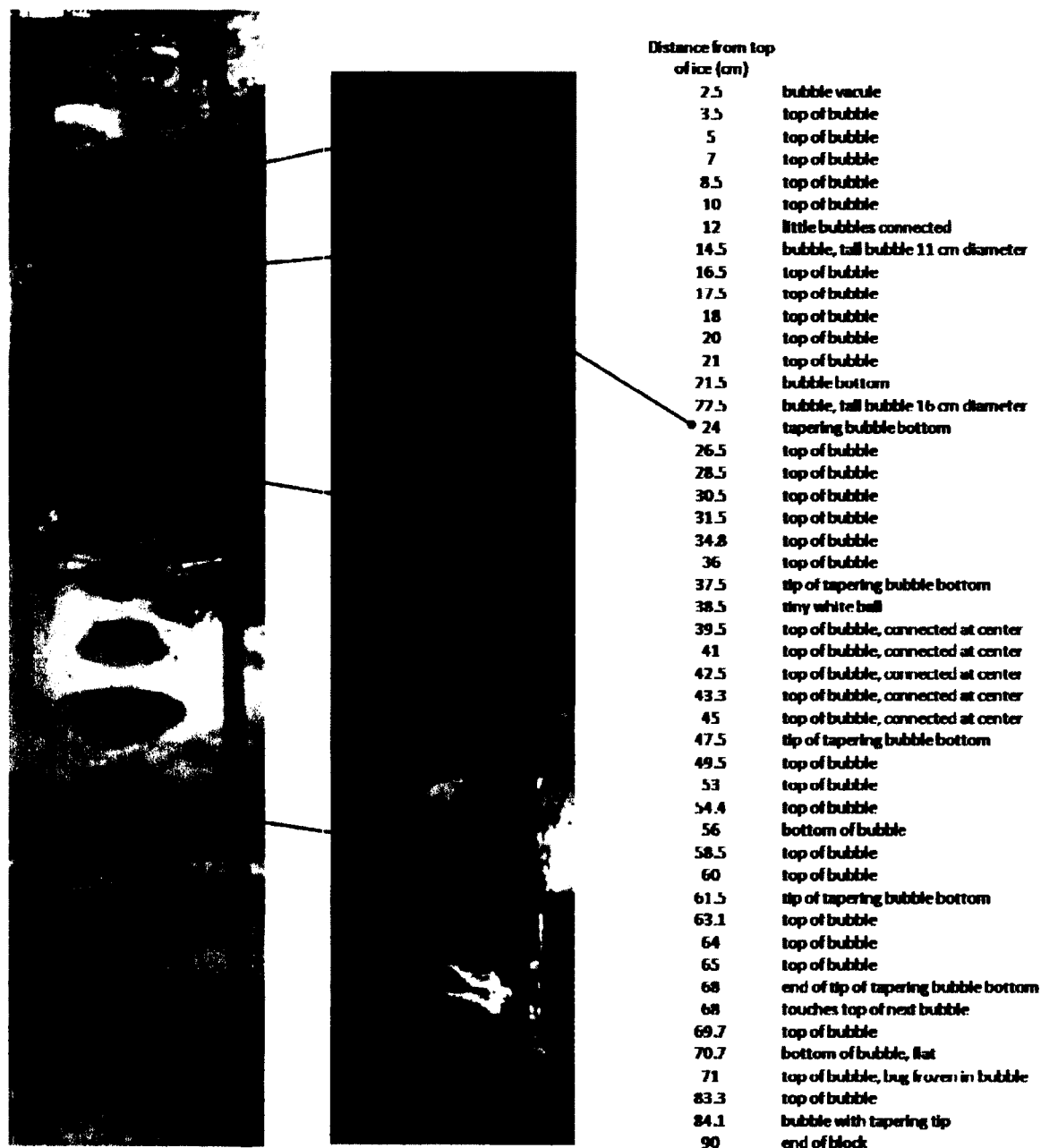


Figure A.2: A vertical column of Type 'A' bubbles as seen from slightly different viewing angles in thick lake ice column. The left photo views the underside of bubbles; the right photo views top and sides of bubbles. Profile measurements from top of ice (cm) are provided on the far right table. Flat circular tops with conical, lenticular, or (rarely), flat bottoms characterize these bubbles which are usually about 1-4 cm in diameter, therefore some of these bubbles are larger than a typical type 'A'. Blue lines link the same bubbles in both photos and chart. Photos by M. Engram.

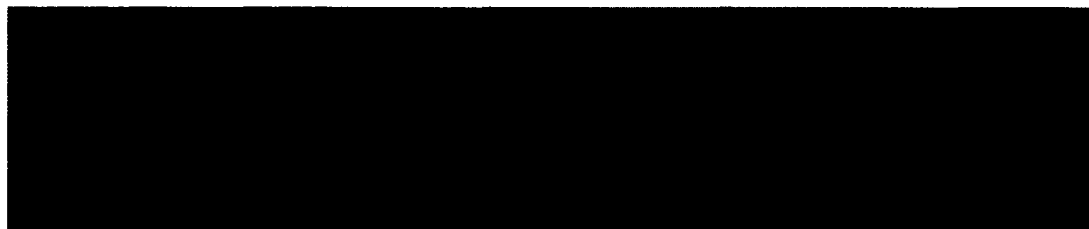


Figure A.3: Dimensions, shape and spacing of small Type 'A' CH₄ bubbles, as viewed from side profile. Note conical or lenticular shape. Color is result of a purple artificial light behind the ice block. Photo by M. Engram.



Figure A.4: Type 'B' bubble cluster with merged bubbles and typical circular "bull's eye" pattern. Photo by M. Engram.

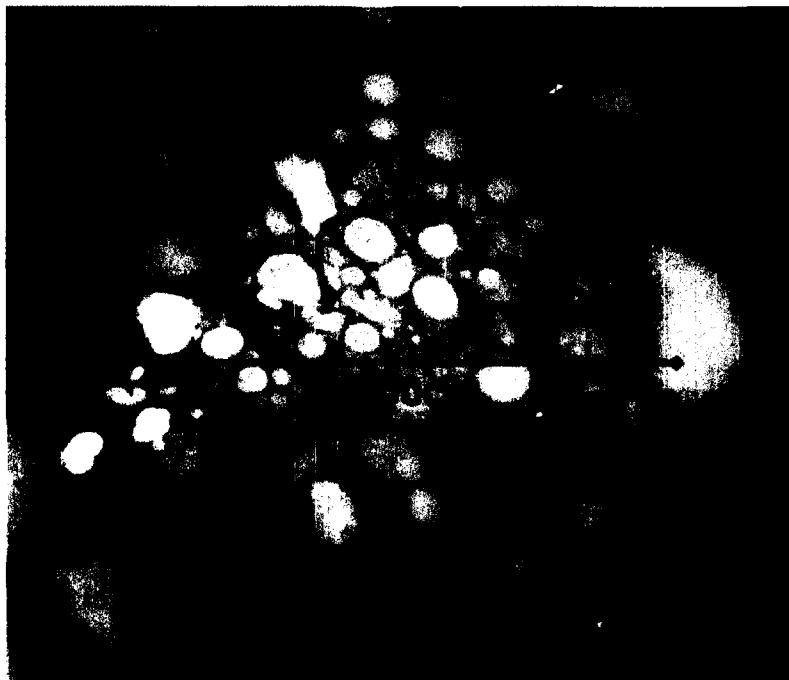


Figure A.5: Type 'B' CH₄ bubble cluster with non-circular pattern. Photo by M. Engram.



Figure A.6: Ice cavity created by strong CH_4 ebullition. This piece of ice was cut from the surface of the lake and inverted for examination. Ridges encircle the main cavity, but are shown most clearly on the left. Ridges measured 1 cm for rise and 1 cm for run and were formed as a result of larger and larger bubbles stacking up underneath the lake ice. Length of blue ruler is 30.48 cm. Photo by M. Engram.

Appendix B: GIS methods for SAR and lake ice analysis

Introduction

The purpose of this appendix is two-fold: 1) to document the methods I used to analyze synthetic aperture radar (SAR) data in a geographic information system (GIS) to estimate methane (CH₄) emissions in thermokarst lakes, as outlined in Chapter 2, and 2) to highlight some 'best practice' approaches that I developed while using SAR in a GIS environment to study lake-source CH₄ emissions. Analyzing SAR data in a geospatial environment using commercial GIS software is a relatively new practice that was greatly facilitated in 2005 when the Alaska SAR Facility (ASF, and since renamed to the Alaska Satellite Facility) unrolled a free software tool suite in 2005, called 'Convert', to ingest SAR data and export a geotiff in a map projection. About the same time, GIS developers from the Leica company added the functionality of importing SAR data to their GIS, ERDAS Imagine, particularly in the .D/.L Level 1 processed data format provided by the ASF. The ability to use SAR data in commercial GIS software applications such as ESRI's ArcMap, ERDAS Imagine and ENVI has created the opportunity for scientists to add SAR as another tool to their scientific investigations by comparing SAR values with field data and with other geospatial data layers.

Type of SAR data and data format

I used SAR data from ASF, both L-band data acquired by the Japan Aerospace exploration Agency's (JAXA) Advanced Land Observing Satellite's (ALOS) Phased-Array type L-band SAR (PALSAR) and C-band data (Table 1) from the European Remote Sensing Satellite 2 (ERS-2). The PALSAR data was in Level 1.5 and Level 1.1 format, as ordered from ASF, with a file structure of at least four files per data granule plus with prefixes: LED, VOL, TRL and

IMG. The ERS-2 data was in Level 1 format with .D and .L files. I used the 'MapReady' software tool from ASF (a successor to the 'Convert' tool) to post-process both L-band and C-band SAR data from ASF to create geotiffs, prior to ingest into GIS.

Geolocation, Seward Peninsula

Geolocation in a SAR analysis is extremely important, since each scene is processed into a visual image, often referred to as a 'detected' image, with the assumption that the ground is flat and the location is at zero elevation above sea-level. Without applying a height correction, a target that is higher than sea level appears with a geolocational shift in the range direction toward nadir (i.e., in the direction perpendicular to the line of flight) in a SAR scene. Targets in the SAR scene will have a geolocational shift unless a digital elevation model (DEM) is used to terrain-correct the image. I attempted to terrain-correct the SAR granules with the best DEM available for the study area, which was the National Elevation Dataset (NED) DEM. The NED DEM has approximately 40 - 60 meter posting, which is much coarser than the SAR data. The NED DEM also had offsets when compared to the coastline. Simple lateral translation of the NED DEM did not result in good co-registration with the ortho-rectified aerial photography of the Seward Peninsula coastline (Manley et al. 2007). In addition I investigated the recently released ASTER GDEM (Advanced Spaceborne Thermal Emission and Reflection Radiometer Global Digital Elevation Model). In this first version of the ASTER GDEM, there was no lake-mask applied, resulting in hill-like artifacts on each lake's surface, which rendered this DEM unusable for lake ice analysis. Also, with 30 m posting, the resolution of the GDEM was still grosser than the SAR data. Since these were the only available DEMs for the Seward Peninsula study site, terrain correction using a DEM would introduce more inaccuracies in the SAR data than it would fix.

Another option to correct the geolocation in SAR data is a constant height correction, where the data are processed assuming a user-supplied constant height above sea level for each image pixel. I tried to use this height correction option in MapReady, but since the lakes were at different heights, constant height correction did not work to georeference all ten study lakes. Using a lake specific height correction for each lake individually would theoretically work to georeference each lake, but we lacked such precise and accurate height information. But even if the precise height for each lake was known, using individual height corrections in MapReady to process SAR data into geotiffs would be so time consuming as to be prohibitive. In addition, the height of the bluffs on many thermokarst lake shores is very different from the height of the lake water, introducing problems in the near-shore zone of lakes with such a method.

Reference data

Finding accurate reference data, i.e., orthorectified images or GPS-surveyed features to use as ground control points is difficult in rural Alaska with few human-made features and few or no accurate, current maps. One of the geospatial challenges of working with thermokarst lakes is that a lake shoreline can dramatically change in the decimeter scale to meter scale in the span of one year (Jones et al. 2011). As thermokarst activity causes slumping and expansion of the lake perimeter, lakes can grow in area quite rapidly and can even merge with other lakes.

Thermokarst lakes can also drain or partly drain, again causing shoreline change. This makes a thermokarst lake shoreline in an older optical image a poor choice for tie points to use with SAR georeferencing. In order to capture the latest shape of the changeable thermokarst lake shorelines I used the most current optical images of the thermokarst lakes in the northern Seward Peninsula: an October, 2008 image from the Panchromatic Remote-sensing Instrument for Stereo Mapping

(PRISM) on ALOS with 2.5 m pixel spacing. Although this 2008 PRISM scene had the most current lake shapes, the geolocation needed confirmation and possible correction. The imagery with the best geolocational accuracy was the 2003 Bering Land Bridge National Preserve (BELA) orthophotos along the coastline (Manley et al. 2007). I refined the geolocation of the 2008 PRISM data showing the current lake perimeters by using ice-wedge polygon junctions as tie points, a method used by Jones et al. (2008), for a lateral translation of about 1 pixel. Using a lateral translation instead of an affine transformation preserved the shape of the lakes. In this way, the most current shoreline location was aligned with the 2003 ortho-rectified aerial imagery using reference points that were independent of changeable shorelines. Field measurements of DGPS occupation of CH₄ bubble location with bubble cluster type and bubble area were accurate within a few centimeters. I then digitized the lake perimeters of the ten study lakes manually in ArcMap (9.2), in UTM zone 3 north, NAD83.

SAR data geolocation

I rectified the SAR data to each lake perimeter, again using lateral translation to avoid distortion of shape of the lakes. I moved a single SAR image to fit each digitized lake perimeter, necessitating the creation of ten files for each SAR scene. In some cases, it was possible to rectify a SAR scene to accurately fit several lakes in the same area with the same height, such as Rhonda, Cocker Gap and Fox Den lakes. This method was the most accurate, yet it created numerous files which added a level of complexity to the project that I mitigated by automating the geoprocessor work flow with Python scripting (section 6). I used the file naming convention to capture information of which lake the scene had been rectified to. Since each rectification was a manual process, I had to be able to see each lake in the SAR scene as differentiated from land,

in order to slide it to the lake perimeter. In the case of some SAR scenes where land and lake ice were at almost the same backscatter value, making it difficult to discern the lake from the land in the SAR image, I used other landmarks in repeat pass SAR scenes with the same geometry (ascending or descending) and similar incidence angles to assist geolocation.

Shoreline buffer distance decision

Since SAR backscatter from pixels near the shoreline could cover both ice and land, it was important to exclude these mixed ice/land pixels when choosing all the pixels that covered a lake. In addition to excluding pixels that represented part land and part ice, in SAR there is a possible adjacency effect from the side lobes of a bright pixel if the side lobes of the bright pixel have a higher value than the main lobe of an adjacent dark pixel. Since the land returns high values compared to the low backscatter values from early lake ice, there is a large contrast along the shore, possibly causing contamination from land side lobes into pixels that geographically cover pure ice. Thirdly, geolocation errors of lakes slightly mis-aligned with their shoreline could cause some brighter land pixels to be erroneously included with the lake-ice pixels for analysis.

For our pilot study (Walter et al. 2008), I excluded pixels that were within the diagonal distance of one pixel from the shore:

$$\text{Buffer distance} = \text{pixel length} * \sqrt{2}$$

I investigated the statistical difference between pixels one pixel distance from the shore and two pixel distances from the shore, using the lakes near Toolik Lake, Alaska, because the Toolik area had much better ground control and more accurate reference data than the northern Seward Peninsula. Since ebullition bubbles in lakes are often denser in the littoral region, their presence could create a true brightening of the ice near shore which would be impossible to separate from

bright contributions from a side-lobe. Thus, I used summer scenes with no ice to test for any shore side-lobes overshadowing lake main-lobes, because a calm lake is a dark, homogenous target against which any 'false' brightening of SAR pixels near shore would be evident. I found a statistical difference between the first ring that included the shoreline and the rest of the lake, using a non-parametric ranking statistical test, but no significant difference that consistently showed up between the second ring and the rest of the lake, nor the third ring and the rest of the lake. I concluded that side-lobes from land pixels were not evident more than one pixel distance from shore.

MapReady processing decisions

I chose nearest neighbor interpolation for resampling during the map projection process because nearest neighbor resampling best preserves the original pixel value without smoothing. This is desirable when evaluating a target with expected variable backscatter values such as lake ice with trapped CH₄ ebullition bubbles, a spatially patchy phenomenon. I used the option to output sigma-naught values in dB for ease in initial investigation. I changed the pixel values from the dB log-scale to powerscale prior to calculating the arithmetic mean.

Python scripts

I wrote scripts in Python (2.6) to automate standard GIS geoprocessing flow in ArcMap (9.2), such as extracting pixels using a buffered shoreline as a 'cookie cutter', converting the raster cells with SAR values for the lake ice to points, adding and calculating fields for the point attribute table and running descriptive statistics (mean, standard deviation, minimum, count, range). The scripts pulled necessary information from each file name which I standardized to include the name of the lake the image had been referenced to, as well as the date and type of

SAR data.

Converting raster to point data

Since the sigma-naught values in SAR data are floating point values, GIS software can't create a value attribute table without first rounding the values to whole numbers. Converting each raster cell to a point, using the Raster to Point Conversion Tool in ArcMap, allows creation of an attribute table with floating point values and allows multiple attributes for one raster cell. With SAR data, it is convenient to have both the powerscale value and the dB value for quick reference. Also, the .dbf file from the point shapefile can be ingested directly into Excel and SPSS, allowing more sophisticated statistical analysis (histograms, kurtosis, box plots, t-tests, ANOVA).

Conclusion

Terrain correction with a DEM that has the same or finer spatial resolution and has sub-SAR-size pixel accuracy would be highly preferable to rectifying each lake individually, but such a DEM does not yet exist for the northern Seward Peninsula study area. There is the possibility of creating a Digital Terrain Model from PRISM triplet data (2.5 m posting), a method that should be evaluated for this type of work in the future. The Alaska Statewide Digital Mapping Initiative (<http://www.alaskamapped.org/>) includes DEM generation for Alaska as part of its goals, so future work using SAR for lake ice analysis could use terrain correction. In the absence of an established best-practice, the distance of the diagonal of one pixel is a starting point for a standard shoreline buffer, since it was sufficient to eliminate any side-lobe bleed-ever effect from bright shore pixels to lake ice pixels.

Appendix B References

- Jones, B.M., Grosse, G., Arp, C.D., Jones, M.C., Anthony, K.M.W., & Romanovsky, V.E. (2011). Modern thermokarst lake dynamics in the continuous permafrost zone, northern Seward Peninsula, Alaska. *Journal of Geophysical Research-Biogeosciences*, 116, G00M03
- Jones, B.M., Hinkel, K.M., Arp, C.D., & Eisner, W.R. (2008). Modern Erosion Rates and Loss of Coastal Features and Sites, Beaufort Sea Coastline, Alaska. *Arctic*, 61, 361-372
- Manley, W.F., Sanzone, D.M., Lestak, L.R., & Parrish, E.G. (2007). High-Resolution Orthorectified Imagery from 2003 for the Coastal Areas of Bering Land Bridge NP (BELA) and Cape Krusenstern NM (CAKR), Northwest Alaska. *Fairbanks, AK: National Park Service, Arctic Network Inventory and Monitoring Program*
- Walter, K.M., Engram, M., Duguay, C.R., Jeffries, M.O., & Chapin, F.S. (2008). The potential use of synthetic aperture radar for estimating methane ebullition from Arctic lake. *Journal of the American Water Resources Association*, 44, 305-315

